

Choice-specific sequences in parietal cortex during a virtual-navigation decision task

Christopher D. Harvey^{1,3,4†}, Philip Coen^{1,4} & David W. Tank^{1,2,3,4}

The posterior parietal cortex (PPC) has an important role in many cognitive behaviours; however, the neural circuit dynamics underlying PPC function are not well understood. Here we optically imaged the spatial and temporal activity patterns of neuronal populations in mice performing a PPC-dependent task that combined a perceptual decision and memory-guided navigation in a virtual environment. Individual neurons had transient activation staggered relative to one another in time, forming a sequence of neuronal activation spanning the entire length of a task trial. Distinct sequences of neurons were triggered on trials with opposite behavioural choices and defined divergent, choice-specific trajectories through a state space of neuronal population activity. Cells participating in the different sequences and at distinct time points in the task were anatomically intermixed over microcircuit length scales (<100 micrometres). During working memory decision tasks, the PPC may therefore perform computations through sequence-based circuit dynamics, rather than long-lived stable states, implemented using anatomically intermingled microcircuits.

In real-world tasks, decision-making and working memory often occur in the context of other complex behaviours, including spatial navigation. For example, when driving through a city towards a destination, sensory information defining context and place engages memory and decision circuits to plan turns at upcoming intersections. The PPC is a prime candidate for the neuronal circuitry combining the cognitive processing elements necessary for such tasks. In primates, the PPC is important for perceptual decision-making and categorization^{1–3}, movement planning⁴ and spatial attention⁵. Studies in rats suggest that the PPC is also important for encoding route progression during navigation^{6–9}. Using a virtual-reality system for mice¹⁰ and cellular resolution optical imaging methods^{11,12}, we developed a T-maze-based navigation task combining all these cognitive elements and characterized the neuronal circuit dynamics in the PPC, which have not been studied in this combined behavioural context.

Neuronal activity patterns in the PPC have been studied using microelectrode recordings during spatial attention, working memory and perceptual decision tasks. These studies have commonly found cells with sustained firing rate changes spanning entire task periods (cue, delay, response periods)^{2,4,5,13}. For example, cells with persistent activity throughout the delay period of memory-guided saccade/reach tasks have frequently been recorded^{14,15}. Also, studies have identified neurons with ramps of increasing firing rate spanning the accumulation of evidence period in a motion perception task¹². Neurons with sustained activity during the same task period often have similar activity time courses, suggesting the presence of classes of cells (for example, delay cells) and implying that the task-dependent neuronal dynamics are low-dimensional. The low-dimensional dynamics can be reproduced in recurrent attractor network models, in which each cell's activity is typically an amplitude-scaled version of a prototypical time series^{16–21}. In contrast, recent analysis of prefrontal cortex activity has identified heterogeneous neuronal activity time courses, in which a neuron's activity can be thought of as the sum of a few activity modes^{22–24}.

In addition, there is growing evidence for sequences of neuronal activation within local circuits, in which each neuron is active for only a fraction of a task period, including during working memory tasks in the prefrontal cortex^{25–28} and the hippocampus²⁹ and during an object construction task in the PPC³⁰. Sequences suggest dynamics that are high-dimensional, without the presence of classes of cells with relatively homogeneous activity time courses.

We explored whether PPC dynamics are best described in terms of cell classes or high-dimensional dynamics. During a navigation-based decision task, the dynamics were high-dimensional: neurons were active in choice-specific sequences in which information moves from one neuronal population to another across time in the task; although the neuronal activity patterns could be divided into cue, delay and response groups, sequences were present within each group. Furthermore, exploiting the ability of cellular resolution optical measurements to provide the relative anatomical location of the recorded cells^{12,31,32}, we found that neurons active during behaviourally distinct task periods and on trials with different behavioural choices were spatially intermixed over microcircuit length scales.

A PPC-dependent navigation-based decision task

Using a virtual-reality system¹⁰, we trained mice to navigate through a virtual T-maze in a task that incorporated both visual discrimination and a memory-guided response (Methods; Fig. 1a). Visual cues present in the initial section of the maze indicated which direction to turn at the T-intersection to receive a water reward (one set of cues to indicate a right turn and a second set for a left turn; Supplementary Fig. 1c). Between the cue section and the T-intersection, mice ran through a delay maze section that was identical on left and right turn trials; visual information about the reward location was thus present only in the cue section. The task resembled traditional delay tasks^{14,15,33} in its cue-delay-response structure, but differed in that continuing sensorimotor activity was present throughout the task, including the delay period.

¹Princeton Neuroscience Institute, Princeton University, Princeton, New Jersey 08544, USA. ²Bezos Center for Neural Circuit Dynamics, Princeton University, Princeton, New Jersey 08544, USA. ³Lewis-Sigler Institute for Integrative Genomics, Princeton University, Princeton, New Jersey 08544, USA. ⁴Department of Molecular Biology, Princeton University, Princeton, New Jersey 08544, USA. [†]Present address: Department of Neurobiology, Harvard Medical School, Boston, Massachusetts 02115, USA.

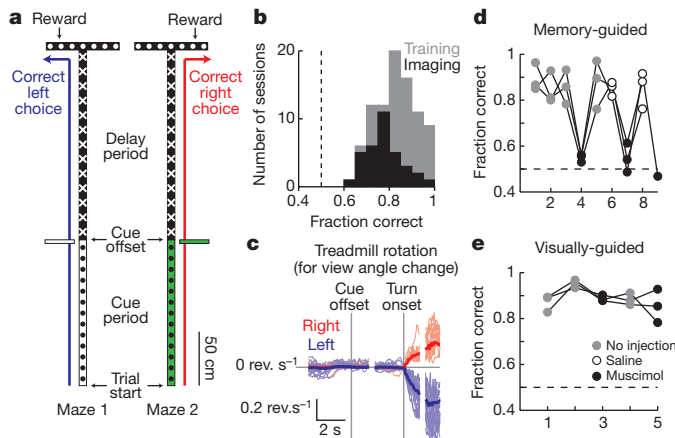


Figure 1 | A PPC-dependent decision task in virtual reality. **a**, Diagram of the two versions of the virtual T-maze that differed only in the cue period and the reward location. Patterns in the diagram reflect the patterns present on the virtual maze walls. **b**, Behavioural performance on individual training (grey) and imaging (black) sessions. **c**, Rotational velocity of the spherical treadmill about the vertical axis for view angle changes on correct right (red) and left (blue) trials, aligned to the cue offset and the turn onset. **d**, Behavioural performance on a memory-guided task from **a** after receiving no injections (grey), saline (open circles) or muscimol (black) bilaterally in the PPC. Connected dots are from individual mice across daily sessions ($n = 3$ mice). **e**, Same as in **d** except for a visually-guided task (Supplementary Fig. 1b; key in **e** applies to **d** also).

Mice performed the task with high levels of accuracy ($83 \pm 9\%$ correct, $P < 0.0001$ versus 50%, t -test; Fig. 1b). Within and across trials, individual mice ran at highly consistent speeds (Supplementary Fig. 2); however, running speeds varied between mice, and the maze position at which mice began rotating the spherical treadmill to make a right or left turn differed across trials (turn onset; Fig. 1c, Supplementary Fig. 3; Methods). To compare behaviourally similar epochs of the task across trials, individual trials were aligned to the time points when the cue was no longer visible (cue offset), the turn onset, and the end of the trial; these alignment points formed the boundaries of cue (trial start to cue offset, 5.1 ± 2.6 s), delay (cue offset to turn onset, 4.2 ± 1.2 s) and turn trial periods (turn onset to trial end, 3.0 ± 1.8 s).

Because the location of the mouse PPC has not been characterized, we first performed retrograde and anterograde labelling experiments to locate it anatomically (Methods, Supplementary Fig. 4). We identified a region consistent with the rat and primate PPC based on the set of areas from where it received axonal projections, the areas to which it sent projections, and its location relative to other cortical regions^{8,34} (anterior to visual cortex and posterior to somatosensory cortex). We therefore considered this area to be the mouse PPC.

To test if the PPC was required for the behavioural task, we inactivated it using bilateral injections of the GABA_A receptor agonist, muscimol. Muscimol reversibly decreased behavioural performance from high levels of accuracy in control sessions to near chance levels, but did not affect the rate of trials performed (fraction correct; no injections $87 \pm 7\%$, saline $85 \pm 5\%$, muscimol $54 \pm 5\%$ $P < 0.0001$ versus no injections, t -test; trials per minute; no injections 3.2 ± 0.5 , muscimol 3.1 ± 0.3 , $P > 0.8$, t -test; Fig. 1d). In contrast, PPC inactivation did not significantly affect performance on a visually guided task in which a visual cue was present at the reward site and visible throughout the trial, indicating that the decrease in performance on the memory-guided task was unlikely to be due to a major visual or motor deficit (fraction correct; no injections, $90 \pm 5\%$; muscimol, $87 \pm 5\%$, $P > 0.2$, t -test; Fig. 1e, Supplementary Fig. 1b).

Imaging sequences of neuronal activity

We used two-photon microscopy to image layer 2/3 PPC neurons expressing the genetically encoded calcium indicator GCaMP3, which

increases in fluorescence intensity in response to action potential firing³⁵ (Methods). On average, we imaged ~ 65 cells simultaneously within an area $\sim 300 \mu\text{m}$ by $\sim 150 \mu\text{m}$ (range, 37–94 cells). Nearly all imaged cells showed statistically significant Ca^{2+} transients during the behavioural session (96% of cells had >0.2 transients per minute; Methods). Of the cells with high levels of activity ($>2 \text{ Ca}^{2+}$ transients per minute on average; Supplementary Fig. 5), $\sim 73\%$ had significant increases in their mean fluorescence intensity traces ($\Delta F/F$, averaged across trials) during a specific time in the trial or inter-trial interval (task-modulated cells; Fig. 2, Supplementary Figs 6, 7). These task-modulated cells had Ca^{2+} transients for only short time intervals on individual trials ($11 \pm 8\%$ of time points in trials with a transient) such that only a small fraction of neurons was active simultaneously (Fig. 2b–e, Supplementary Figs 8, 9a); cells with prolonged activity patterns covering a large fraction of the trial were not observed. The majority ($\sim 71\%$) of task-modulated cells had significantly different levels of activity on correct right and left choice trials (choice-specific cells). Similar choice-specific, task-modulated activity patterns were observed in extracellular electrophysiological recordings (Supplementary Figs 10, 11). Cells were also active on error trials, such that neurons active during the cue period tended to be correlated with the cue identity, and neurons active during the turn period in general were correlated with the behavioural response (Supplementary Fig. 12). Only a small fraction of cells had obvious reward-related signals ($\sim 2\%$ of active cells with $P < 0.01$, t -test, comparing $\Delta F/F$ values within ~ 0.6 s after the reward was given on correct trials or missed on error trials).

When the activity patterns of all the choice-specific, task-modulated cells were ordered according to the time profile of their Ca^{2+} transients, the active periods across cells were staggered relative to one another in time, forming a sequence of neuronal activation covering the entire trial length (Fig. 2c, d, Supplementary Fig. 7c). Different sequences of neurons were activated on left and right trials (Fig. 2c, d and absence of activity in Fig. 2d lower plot, Supplementary Fig. 14e). Although these plots of sequences combined cells from different experiments and averaged across trials, similar properties were observed when considering only the cells imaged in a single mouse and on individual trials (Fig. 2c, Supplementary Fig. 13). Sequences were also apparent in the $\sim 29\%$ of task-modulated cells that did not have choice-specific activity; these cells participated in the sequences for both right and left choice trials (Supplementary Fig. 7b). In total, $\sim 73\%$ of the highly active cells participated in sequences. Sequences similar to those during the task were not observed in shuffled versions of the data set, demonstrating that the sequences were not an artefact created by ordering the data (Supplementary Fig. 14a–d).

Because previous studies of the PPC have categorized cells into classes with cue, delay or response period activity^{14,15}, we examined the activity patterns to see if neurons in the sequence were grouped on the basis of behavioural periods. The distribution of activity times of all cells in the population (calculated for each cell as the centre-of-mass (COM) in time of the mean $\Delta F/F$ during the trial, t_{COM}) had three peaks corresponding to the cue, delay and turn periods, suggesting a possible grouping by behavioural period (Fig. 3a). Consistently, principal component analysis (PCA) of the mean $\Delta F/F$ traces for all cells revealed three intermixed groups, with each group mostly containing cells preferring the same behavioural period (Fig. 3a, b, Supplementary Fig. 15).

Although the population of neurons could be divided into groups, the temporal activity patterns within each individual period were heterogeneous and formed sequences (Fig. 3c). Cells within their preferred period were active for only a fraction of the period ($35 \pm 16\%$ of time points in preferred periods with a Ca^{2+} transient), with different cells active at different times. Although cells with activity covering a large fraction of the period were occasionally observed (for example, Fig. 2c top panel), these cells were rare (4% of cells with activity lasting for $>60\%$ of the period; Supplementary Fig. 9b); the distribution of

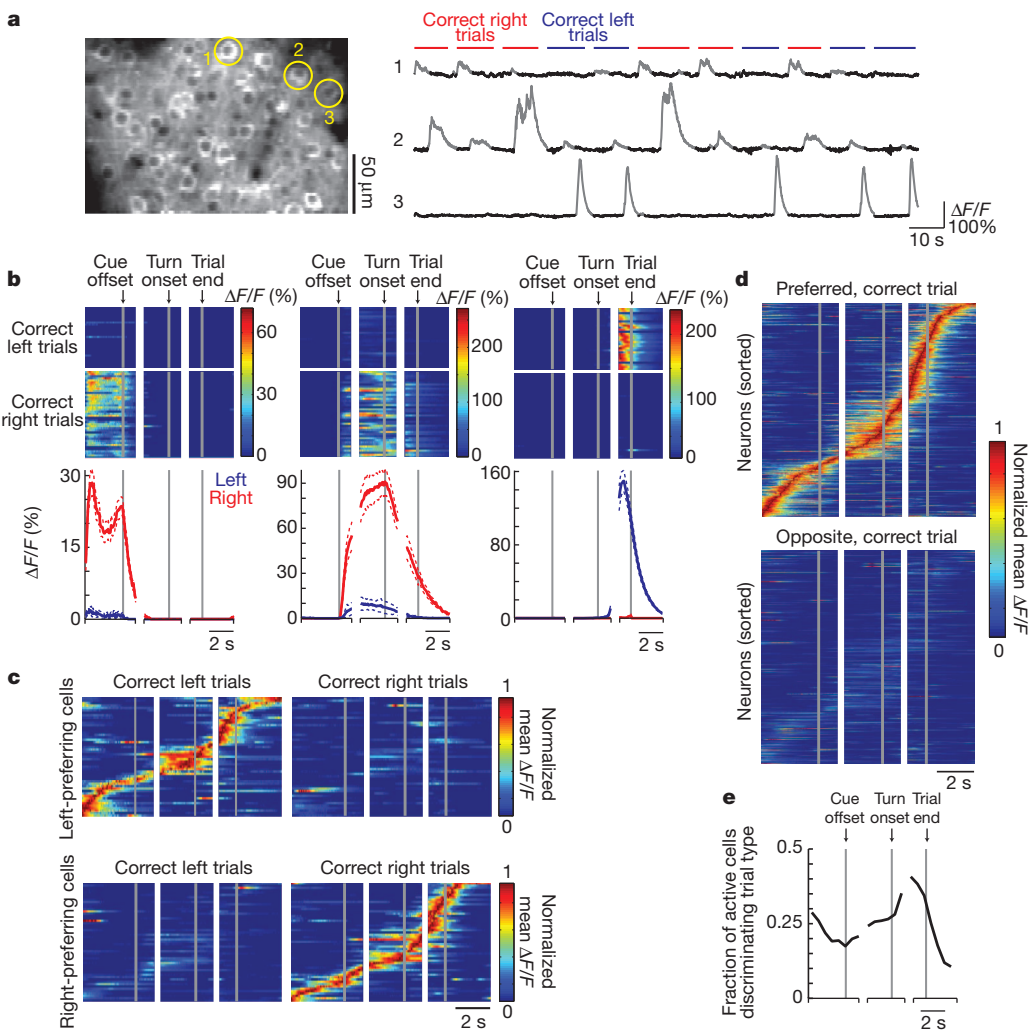


Figure 2 | Imaging PPC neuronal activity during the T-maze task. **a**, Left: example image of GCaMP3-expressing neurons in layer 2/3. Right: example fluorescence intensity traces ($\Delta F/F$; grey portions indicate significant Ca^{2+} transients, Methods) for three example cells from the left panel on correct right (red) and left (blue) trials. **b**, Activity patterns during the task for cells 1–3 from **a**. Top: colour-coded $\Delta F/F$ traces for individual correct left and right choice trials. Each row is a single trial aligned to the cue offset, turn onset and trial end. Bottom: mean $\Delta F/F$ traces for correct right (red) and left (blue) choice trials. Dashed lines indicate mean \pm s.e.m. **c**, Normalized mean $\Delta F/F$ traces for all the

epoch coverage by an individual neuron's activity was similar during the delay and cue or turn periods ($P > 0.1$, Kolmogorov-Smirnov test). Furthermore, Pearson's correlations between the non-averaged $\Delta F/F$ traces for cell pairs with the same trial-type and behavioural period preferences varied widely, with a large fraction of pairs having low correlation coefficients (Supplementary Fig. 16a). The low correlation coefficients could be due to activity at different times in the period, as expected for sequences, or activity at the same time in the trial except on different trials. However, the probability that both cells in these pairs had Ca^{2+} transients or that both cells did not have transients on the same trial during their preferred epoch was generally high (Supplementary Fig. 16b), suggesting that the diversity primarily resulted from differences in the activity times of cells within trials. Together these data indicate that classes of cells with homogeneous activity patterns were not present. Rather, choice-specific sequences of neurons were activated in all behavioural periods, with a lower density of cells in the sequence at the borders between periods.

To further examine the sequential neuronal activation on individual trials, we calculated correlations between the activity patterns of cells using the non-averaged $\Delta F/F$ time series. Cells that were active

choice-specific, task-modulated cells (one cell per row) imaged in a single mouse and divided by left-prefering ($n = 51$) and right-prefering ($n = 54$) cells. Traces were normalized to the peak of each cell's mean $\Delta F/F$ trace on preferred trials and sorted by the peak time. Some cells were imaged on different days and in different fields-of-view. **d**, Same as in **c**, except for all mice ($n = 404$ cells from 6 mice) on preferred and opposite trials. **e**, Fraction of active cells with significantly different activity levels on right and left choice trials as a function of trial time.

at similar time points in the trial on average (measured as the difference in t_{COM} values on correct trials, Δt_{COM}) had, on correct trials and in their preferred behavioural periods, highly correlated $\Delta F/F$ traces and peaks in their cross-correlation at a lag approximately equal to Δt_{COM} (Supplementary Fig. 16d–h); these relationships in the non-averaged $\Delta F/F$ time series provide further evidence for sequential activity on individual trials. Cells that were active at similar times on correct trials were also highly correlated on error trials and in non-preferred periods (Supplementary Fig. 16c–f). Additionally, cells that were sequentially activated during their preferred behavioural period on correct trials were sequentially active with similar lags during error trials and other time points in the task (Supplementary Fig. 16g–i).

The choice-specific activity could result if mice experienced different visual stimuli and running patterns on right and left trials and if PPC activity was modulated by those differences. To examine this, we first performed a multiple regression analysis to determine the potential effects of the parameters defining the mouse's running trajectory on the fluorescence changes during the delay period (Supplementary Table 1). These parameters could not explain the choice-specific

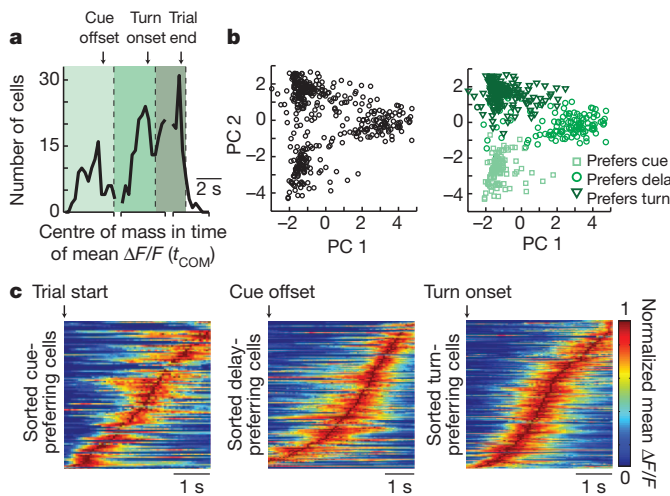


Figure 3 | Neuronal activity in individual behavioural periods. **a**, Histogram of the times of the centre-of-mass of the mean $\Delta F/F$ trace (t_{COM}) for choice-specific, task-modulated cells. Cells were separated into three groups (cue-, delay- and turn-preferring cells; varying shades of green) based on peaks in the distribution. **b**, PCA on the normalized mean $\Delta F/F$ traces for all the choice-specific, task-modulated cells. Left, scores for each cell plotted for the first two principal components (PC 1, 2). Right, cells categorized on the basis of groupings from **a**. $n = 404$ cells. **c**, Sorted normalized mean $\Delta F/F$ traces for cue-preferring ($n = 101$), delay-preferring ($n = 133$) and turn-preferring ($n = 170$) cells, aligned to the trial start, cue offset and turn onset, respectively, on the preferred trial-type.

activity patterns, suggesting that any differences in running trajectories between right and left trials did not trigger the activity we observed. In addition, we performed two sets of experiments to further examine whether the maze visual stimuli alone or the mouse's running patterns triggered PPC activity. In the first experiments, movies of simulated left and right turn runs through the T-maze, which closely approximated real runs, were played to mice that passively viewed the visual scenes (open-loop experiments; Supplementary Fig. 17a, b). In the second experiments, mice were trained on a virtual linear track to perform a simple running back and forth task (run to one end for a reward, turn around, run to the other end for the next reward). The linear track had several visual patterns on the walls, all of which were the same as patterns in portions of the T-maze (Supplementary Fig. 18a, b). The task required similar running and turning behaviours to the T-maze, except that turns were not memory-guided based on visual cues and a delay period, and there was not a two-alternative forced-choice structure. The overall levels of activity during the simulated T-maze runs or during the linear track task were much lower than when mice actively performed the T-maze task (Supplementary Figs 17c, d, 18c, d). Also, only a small fraction of neurons had significant increases in activity at specific locations in the maze, either during the simulated T-maze runs or in the linear track, suggesting that cells were not activated robustly by location-specific visual scenes or running patterns (simulated runs, 1.3% of neurons; linear track, 5.8%; T-maze, 32.3%; Supplementary Figs 17e–k, 18e–k). Together these results suggest that PPC neurons in the T-maze were not activated only by the visual information or by the running patterns of the mouse.

Choice-specific neuronal circuit trajectories

The heterogeneous and sequential neuronal activity patterns during the T-maze task indicated that we should consider the dynamics of the population rather than classes of cells. We therefore analysed the dynamics as a trajectory through a state space of neuronal population activity (neuronal circuit trajectory)^{36–38}. At each time point, the activity state of the circuit containing n simultaneously imaged neurons was defined as a point in an n -dimensional space, with each dimension representing the activity ($\Delta F/F$ values) of a single neuron. Different

trajectories (visualized using factor analysis for dimensionality reduction) were traversed for trials with different behavioural choices (Fig. 4a, b, Supplementary Fig. 19a). The trajectories for correct right and left choice trials began the trial at similar positions, gradually diverged to reach a peak separation near the time of the behavioural choice, and converged to the starting point in the inter-trial interval (Fig. 4a–d). To quantify the trajectory divergence, we used a classifier based on the distance from an individual trial trajectory to the mean right and left choice trajectories at single time points. It was possible, from the activity of a small population of neurons located in close anatomical proximity (~ 65 neurons separated by $<250 \mu\text{m}$), to predict the mouse's choice on single correct trials at better than chance levels during the cue, delay and turn periods (Methods; Fig. 4e, Supplementary Fig. 19b, c). The activity in the PPC can therefore be considered as divergent, choice-specific trajectories through a state space of neuronal population activity.

Trajectories were highly variable on error trials. Some trajectories began close to the correct choice trajectory during the cue period and

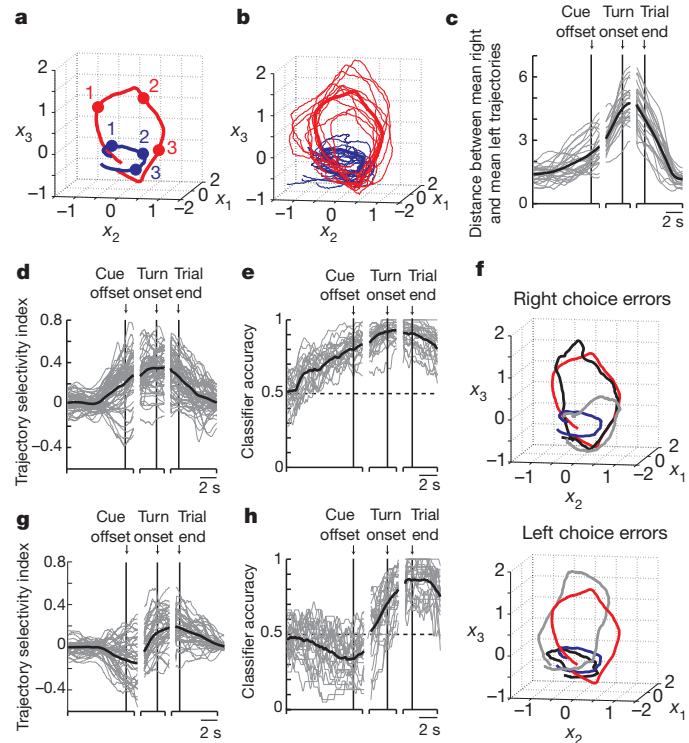


Figure 4 | Neuronal circuit trajectories on correct and error trials. **a**, Time course of mean choice-specific trajectories on correct right (red) and left (blue) choice trials from one session (plotted for the first three common factors). Points labelled 1, 2 and 3 correspond to the mean times of the cue offset, turn onset and trial end, respectively. **b**, Example individual (thin lines) and mean (thick lines) trajectories for correct trials from the session in **a**. **c**, Euclidean distance between the mean trajectories on correct right and left choice trials ($n = 29$ individual sessions, grey). The black line indicates the mean. **d**, Trajectory selectivity index for individual correct trials from a single session, defined on the basis of distances as $(d_{\text{to mean traj, opposite choice}} - d_{\text{to mean traj, same choice}})/(d_{\text{to mean traj, same choice}} + d_{\text{to mean traj, opposite choice}})$. Values close to 1 and -1 indicate that the individual trial trajectory was near the mean trajectory of the same and the opposite behavioural choice, respectively. Mean trajectories were defined using correct trials only. Grey and black lines indicate individual trials and the mean, respectively. **e**, Classification accuracy for determining the behavioural choice of the mouse at different time points in the task during individual sessions ($n = 29$; black, mean). The classifier was based on a distance-dependent classification scheme (see Methods) using correct trials. **f**, Example individual trial trajectories (grey and black) on right choice and left choice errors trials, plotted with the mean trajectories for correct right (red) and left (blue) choice trials. **g**, Same as for **d**, except on error trials. **h**, Same as for **e**, except on error trials.

transitioned towards the error choice trajectory later in the trial; such transitions occurred at a wide range of points in the trial (grey traces in Fig. 4f, Supplementary Fig. 19f). Other trajectories were similar to the error choice trajectory throughout the trial (Fig. 4f, black traces). On average, the error trial trajectories were more similar to the correct choice trajectory during the cue period and closer to the error choice trajectory during the turn period (cue offset; trajectory selectivity index = -0.13 ± 0.22 , $P < 0.001$ versus 0, *t*-test; trial end; trajectory selectivity index = 0.18 ± 0.15 , $P < 0.001$ versus 0; Fig. 4g; consistent results based on classification, Fig. 4h). Therefore, individual trajectories transitioned between the mean correct right and left choice trajectories at many time points during trials, but most frequently switched during the delay period.

Anatomical micro-organization of PPC dynamics

To determine how the cells implementing the activity dynamics were anatomically organized, we first examined the neuronal activity patterns to see if cells with different response preferences, such as activity peaks at different times in the trial or different preferences for right and left choice trials, were present in the same regions of the PPC or separated into different areas. Each $\sim 250 \mu\text{m}$ by $\sim 125 \mu\text{m}$ area (that is, field-of-view with simultaneously imaged cells) contained both right and left choice-preferring cells of approximately equal numbers and cells with activity peaks at a wide range of times in the trial (Fig. 5a–c, Supplementary Fig. 20). Next, within each imaged area we compared the activities of pairs of neurons as a function of the distance between the neurons' cell bodies. The difference in the trial-type selectivity for cells in a pair did not depend significantly on the distance between cells, indicating that left and right choice-preferring cells were intermixed ($\rho = 0.04$, Spearman's correlation, $P > 0.05$; Fig. 5e). Similarly, Δt_{COM}

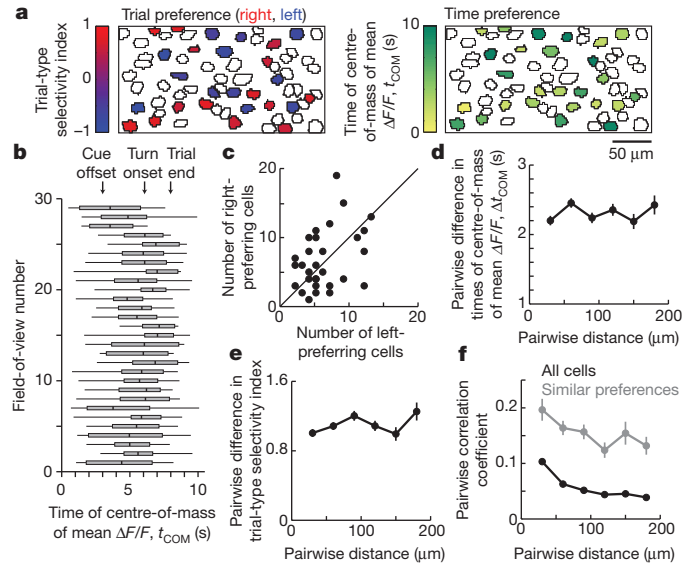


Figure 5 | Anatomical micro-organization in the PPC. **a**, Example field-of-view with cells outlined and choice-specific, task-modulated cells coloured. Left, cells' trial-type selectivity, defined as $(\Delta F/F_{\text{right trials}} - \Delta F/F_{\text{left trials}})/(\Delta F/F_{\text{right trials}} + \Delta F/F_{\text{left trials}})$. Values close to 1 (red) and -1 (blue) indicate right and left choice preferences, respectively. Right, cells' time of the centre-of-mass of the mean $\Delta F/F$ trace (t_{COM}). $t_{\text{COM}} = 0$ corresponds to ~ 3 s before the cue offset. **b**, Box plots of t_{COM} values for task-modulated cells in individual fields-of-view (box edges, first and third quartiles; vertical line in the box, median; whiskers, range). **c**, Number of right and left choice-preferring cells in each field-of-view ($n = 29$; unity line is shown). **d**, Difference in t_{COM} as a function of the distance between cells. **e**, Difference in the trial-type selectivity index as a function of the distance between cells. **f**, Pearson's correlation between non-averaged $\Delta F/F$ traces (all time points) for all pairs of active cells (black) and cell pairs with the same trial-type and behavioural period preference (grey) as a function of the cell-cell distance.

for a cell pair did not differ with the distance between the cells, indicating that cells active during different periods of the task were intermingled ($\rho = -0.01$, $P > 0.6$; Fig. 5d). However, cells that were separated by less anatomical distance had $\Delta F/F$ traces that were significantly more correlated than cell pairs further apart, but the relationship between the correlation coefficient and distance was weak (all pairs of active cells; $\rho = -0.16$, $P < 0.001$; pairs with the same trial-type and behavioural period preference; $\rho = -0.22$, $P < 0.001$; Fig. 5f). This weak relationship could be due to overlapping fluorescence changes, such as from dendritic signals, or could reflect an actual, weak spatial organization. Regardless, cells with highly different activity patterns were intermixed over short length scales, and an anatomical separation of the response properties we measured was not present.

Discussion

The choice-specific sequences of PPC neuronal activation we report here add to the growing list of studies that have identified cortical sequences of activity states during working memory tasks^{27–30}. Furthermore, because we demonstrated that PPC activity was necessary only for the memory-guided task, the sequences of activation were probably important at least for the memory aspect of the task. Sequence-based dynamics may therefore be a common framework for circuit function during memory and decision tasks, including during navigation behaviours. Such dynamics could potentially be implemented using feedforward architectures^{39,40} or liquid state machines^{41,42} related to those that have been proposed for working memory.

Our results also offer a way to unite previous work on neural coding in the PPC. Navigation, memory and choice information may be combined in the sequences such that the identity of the active sequence reflects choice-related information for working memory and movement planning^{4,5}, and that the currently active cell within the sequence reflects spatial or temporal progression through the task^{7,43}, which were highly correlated in our task (Supplementary Fig. 2). It seems unlikely that PPC neurons only provided location information in a context-dependent manner, like hippocampal place cells^{29,44}, because unlike place cells PPC neurons did not encode spatial location during a linear track task (Supplementary Fig. 18) or other tasks^{6,7}.

A possible explanation for heterogeneity and sequences in our experiments versus stereotypy and low-dimensional dynamics, which have been emphasized in previous recordings and models of PPC activity^{1,13–18,20,21}, is that the PPC adopts different dynamics depending on the demands of the behavioural task. Because traditional delayed saccade tasks, for example, have one spatiotemporal component during the delay period (fixation before making a response), the PPC may adopt sustained activity patterns. In contrast, during tasks that involve many spatial and temporal components, as are common in natural behaviours and during navigation, the PPC may utilize sequences of activation. Alternatively, sequences of activity may be present in the primate PPC during traditional tasks but have yet to be identified, consistent with emerging evidence for heterogeneous temporal response properties^{22–24,30}. In addition, different regions or layers of the PPC may have differing activity dynamics⁴⁵, or the dynamics of rodent and primate PPC circuits may differ.

Because cells that were active at distinct time points in the task and that participated in different choice-specific sequences were spatially intermingled, our results indicate that functionally distinct sub-networks are anatomically interlaced in the PPC. This extends previous work in sensory cortex, motor cortex and the hippocampus showing spatial intermixing of heterogeneous response properties in cells encoding qualitatively similar types of information (for example, orientation selectivity in visual cortex) or in cells with activity during similar task epochs^{12,31,32}. Our findings differ from the predictions of models that have emphasized the spatial clustering of similar response patterns, as in functional columns, and that propose connectivity defined by axonal–dendritic overlap without fine-scale specificity^{46,47}. Rather, our results support a model in which microcircuits are formed

by highly specific synaptic connectivity and are composed of neuronal motifs, such as those identified in brain slice recordings in sensory cortices^{48,49} and amongst visual cortical neurons with the same orientation selectivity⁵⁰. Our results showing that cell pairs that were sequentially active during their preferred periods on correct trials had similar activity relationships even during error trials and the inter-trial interval suggest the presence of such motifs (Supplementary Fig. 16g–i).

The behavioural task used here did not isolate the decision-making process. We note however that activity trajectories occasionally switched during a trial between the prototypical correct left and right choice trajectories, including frequently on error trials, suggesting that the mouse's decision was not necessarily irreversibly reached immediately after a trial's start (trajectory selectivity switch during the delay period or last 1 s of the cue period; 63% of error trials, 20% of correct trials; Fig. 4d, g, Supplementary Fig. 19e, f). Sequences may therefore play a role in some aspect of decision-related processes, but further experiments will be necessary to assess this possibility.

Our results motivate consideration of a conceptual framework for decision-making and working memory in which sensory information used for the decision activates a neuronal sequence of activity. The sequence begins in a choice-independent state, which could be mediated by neurons that are not choice-specific (Supplementary Fig. 7b), and then moves towards a choice-specific trajectory and away from other trajectories in a manner dependent on the incoming information. A decision is proposed to be reached when the sequence of activity intersects a choice-specific trajectory; different decisions involve intersections with different trajectories. Upon reaching a decision, a working memory can be maintained by continuing along that choice-specific trajectory. Changing decisions would occur through transitions between trajectories, but as time progresses in the task, the state space distance between trajectories increases, in effect creating a larger barrier to change. In this view, decision-making and working memory utilize an ordered progression through a sequence in which information moves from one population of neurons to another over time. The framework we propose is an extension of a point-of-view first considered in describing the dynamics underlying behavioural choices in the leech nervous system³⁷. It has some similarities with (and some differences from) drift/diffusion-to-bound, race, and recurrent network models of decision-making implemented as neuronal integrator winner-take-all circuits^{2,16}. These models are similar to the trajectory-based view in that different decisions correspond to a divergence in state space surrounding a separatrix. However, these models differ from the sequence framework in that decisions are reached when the activity approaches a choice-specific fixed point with working memory maintained as stable activity at that point. Thus, although these circuits can demonstrate divergent trajectories to reach the fixed points associated with different choices, the trajectories are defined by relatively homogeneous changes in the activity of the population, and the same set of neurons participate in all stages of the decision-making and working memory process.

METHODS SUMMARY

Using a previously described virtual-reality system¹⁰, male C57/BL6 mice were trained using operant conditioning to navigate through a virtual T-maze to receive water rewards. Translation and rotation in the virtual environment were controlled by the mouse's running on a spherical treadmill. Training was performed using shaping implemented as a set of six mazes of increasing task difficulty. Retrograde tracing was performed using fluorescent beads, and anterograde tracing was performed following injections of adeno-associated virus (AAV) containing GFP or GCaMP3. Muscimol injections for PPC inactivation were made bilaterally $\sim 350 \mu\text{m}$ beneath the dura (50 nl, 1 ng nl^{-1}). Imaging was performed using a custom two-photon microscope incorporated with the virtual-reality system, as described previously¹². Imaging occurred at 2–6 weeks after injection of AAV2/1-synapsin-1-GCaMP3 virus³⁵. A complete description of the experimental methods and data analysis is available in the Supplementary Information.

Received 5 December 2011; accepted 2 February 2012.

Published online 14 March 2012.

- Shadlen, M. N. & Newsome, W. T. Neural basis of a perceptual decision in the parietal cortex (area LIP) of the rhesus monkey. *J. Neurophysiol.* **86**, 1916–1936 (2001).
- Gold, J. I. & Shadlen, M. N. The neural basis of decision making. *Annu. Rev. Neurosci.* **30**, 535–574 (2007).
- Freedman, D. J. & Assad, J. A. A proposed common neural mechanism for categorization and perceptual decisions. *Nature Neurosci.* **14**, 143–146 (2011).
- Andersen, R. A. & Cui, H. Intention, action planning, and decision making in parietal-frontal circuits. *Neuron* **63**, 568–583 (2009).
- Bisley, J. W. & Goldberg, M. E. Attention, intention, and priority in the parietal lobe. *Annu. Rev. Neurosci.* **33**, 1–21 (2010).
- McNaughton, B. L. et al. Cortical representation of motion during unrestrained spatial navigation in the rat. *Cereb. Cortex* **4**, 27–39 (1994).
- Nitz, D. A. Tracking route progression in the posterior parietal cortex. *Neuron* **49**, 747–756 (2006).
- Whitlock, J. R., Sutherland, R. J., Witter, M. P., Moser, M. B. & Moser, E. I. Navigating from hippocampus to parietal cortex. *Proc. Natl Acad. Sci. USA* **105**, 14755–14762 (2008).
- Calton, J. L. & Taube, J. S. Where am I and how will I get there from here? A role for posterior parietal cortex in the integration of spatial information and route planning. *Neurobiol. Learn. Mem.* **91**, 186–196 (2009).
- Harvey, C. D., Collman, F., Dombeck, D. A. & Tank, D. W. Intracellular dynamics of hippocampal place cells during virtual navigation. *Nature* **461**, 941–946 (2009).
- Dombeck, D. A., Khabbaz, A. N., Collman, F., Adelman, T. L. & Tank, D. W. Imaging large-scale neural activity with cellular resolution in awake, mobile mice. *Neuron* **56**, 43–57 (2007).
- Dombeck, D. A., Harvey, C. D., Tian, L., Looger, L. L. & Tank, D. W. Functional imaging of hippocampal place cells at cellular resolution during virtual navigation. *Nature Neurosci.* **13**, 1433–1440 (2010).
- Curtis, C. E. & Lee, D. Beyond working memory: the role of persistent activity in decision making. *Trends Cogn. Sci.* **14**, 216–222 (2010).
- Barash, S., Bracewell, R. M., Fogassi, L., Gnadt, J. W. & Andersen, R. A. Saccade-related activity in the lateral intraparietal area. I. Temporal properties; comparison with area 7a. *J. Neurophysiol.* **66**, 1095–1108 (1991).
- Chafee, M. V. & Goldman-Rakic, P. S. Matching patterns of activity in primate prefrontal area 8a and parietal area 7ip neurons during a spatial working memory task. *J. Neurophysiol.* **79**, 2919–2940 (1998).
- Wang, X. J. Decision making in recurrent neuronal circuits. *Neuron* **60**, 215–234 (2008).
- Wong, K. F. & Wang, X. J. A recurrent network mechanism of time integration in perceptual decisions. *J. Neurosci.* **26**, 1314–1328 (2006).
- Mazurek, M. E., Roitman, J. D., Ditterich, J. & Shadlen, M. N. A role for neural integrators in perceptual decision making. *Cereb. Cortex* **13**, 1257–1269 (2003).
- Ganguly, S. et al. One-dimensional dynamics of attention and decision making in LIP. *Neuron* **58**, 15–25 (2008).
- Miller, P., Brody, C. D., Romo, R. & Wang, X. J. A recurrent network model of somatosensory parametric working memory in the prefrontal cortex. *Cereb. Cortex* **13**, 1208–1218 (2003).
- Machens, C. K., Romo, R. & Brody, C. D. Flexible control of mutual inhibition: a neural model of two-interval discrimination. *Science* **307**, 1121–1124 (2005).
- Machens, C. K., Romo, R. & Brody, C. D. Functional, but not anatomical, separation of "what" and "when" in prefrontal cortex. *J. Neurosci.* **30**, 350–360 (2010).
- Jun, J. K. et al. Heterogenous population coding of a short-term memory and decision task. *J. Neurosci.* **30**, 916–929 (2010).
- Singh, R. & Eliasmith, C. Higher-dimensional neurons explain the tuning and dynamics of working memory cells. *J. Neurosci.* **26**, 3667–3678 (2006).
- Batuev, A. S. Two neuronal systems involved in short-term spatial memory in monkeys. *Acta Neurobiol. Exp. (Warsz.)* **54**, 335–344 (1994).
- Seidemann, E., Meilijison, I., Abeles, M., Bergman, H. & Vaadia, E. Simultaneously recorded single units in the frontal cortex go through sequences of discrete and stable states in monkeys performing a delayed localization task. *J. Neurosci.* **16**, 752–768 (1996).
- Baeg, E. H. et al. Dynamics of population code for working memory in the prefrontal cortex. *Neuron* **40**, 177–188 (2003).
- Fujisawa, S., Amarasingham, A., Harrison, M. T. & Buzsaki, G. Behavior-dependent short-term assembly dynamics in the medial prefrontal cortex. *Nature Neurosci.* **11**, 823–833 (2008).
- Pastalkova, E., Itskov, V., Amarasingham, A. & Buzsaki, G. Internally generated cell assembly sequences in the rat hippocampus. *Science* **321**, 1322–1327 (2008).
- Crowe, D. A., Averbeck, B. B. & Chafee, M. V. Rapid sequences of population activity patterns dynamically encode task-critical spatial information in parietal cortex. *J. Neurosci.* **30**, 11640–11653 (2010).
- Ohki, K., Chung, S., Ch'ng, Y. H., Kara, P. & Reid, R. C. Functional imaging with cellular resolution reveals precise micro-architecture in visual cortex. *Nature* **433**, 597–603 (2005).
- Komiyama, T. et al. Learning-related fine-scale specificity imaged in motor cortex circuits of behaving mice. *Nature* **464**, 1182–1186 (2010).
- Erlich, J. C., Blaak, M. & Brody, C. D. A cortical substrate for memory-guided orienting in the rat. *Neuron* **72**, 330–343 (2011).

34. Corwin, J. V. & Reep, R. L. Rodent posterior parietal cortex as a component of a cortical network mediating directed spatial attention. *Psychobiology* **26**, 87–102 (1998).
35. Tian, L. *et al.* Imaging neural activity in worms, flies and mice with improved GCaMP calcium indicators. *Nature Methods* **6**, 875–881 (2009).
36. Mazor, O. & Laurent, G. Transient dynamics versus fixed points in odor representations by locust antennal lobe projection neurons. *Neuron* **48**, 661–673 (2005).
37. Briggman, K. L., Abarbanel, H. D. & Kristan, W. B. Jr. Optical imaging of neuronal populations during decision-making. *Science* **307**, 896–901 (2005).
38. Churchland, M. M., Yu, B. M., Sahani, M. & Shenoy, K. V. Techniques for extracting single-trial activity patterns from large-scale neural recordings. *Curr. Opin. Neurobiol.* **17**, 609–618 (2007).
39. Goldman, M. S. Memory without feedback in a neural network. *Neuron* **61**, 621–634 (2009).
40. Ganguli, S., Huh, D. & Sompolinsky, H. Memory traces in dynamical systems. *Proc. Natl Acad. Sci. USA* **105**, 18970–18975 (2008).
41. Maass, W., Joshi, P. & Sontag, E. D. Computational aspects of feedback in neural circuits. *PLOS Comput. Biol.* **3**, e165 (2007).
42. Sussillo, D. & Abbott, L. F. Generating coherent patterns of activity from chaotic neural networks. *Neuron* **63**, 544–557 (2009).
43. Leon, M. I. & Shadlen, M. N. Representation of time by neurons in the posterior parietal cortex of the macaque. *Neuron* **38**, 317–327 (2003).
44. Wood, E. R., Dudchenko, P. A., Robitsek, R. J. & Eichenbaum, H. Hippocampal neurons encode information about different types of memory episodes occurring in the same location. *Neuron* **27**, 623–633 (2000).
45. Burke, S. N. *et al.* Differential encoding of behavior and spatial context in deep and superficial layers of the neocortex. *Neuron* **45**, 667–674 (2005).
46. Braintenberg, V. B. & Schutz, A. *Anatomy of the Cortex: Statistics and Geometry* (Springer, 1991).
47. Binzegger, T., Douglas, R. J. & Martin, K. A. A quantitative map of the circuit of cat primary visual cortex. *J. Neurosci.* **24**, 8441–8453 (2004).
48. Yoshimura, Y., Dantzker, J. L. & Callaway, E. M. Excitatory cortical neurons form fine-scale functional networks. *Nature* **433**, 868–873 (2005).
49. Song, S., Sjostrom, P. J., Reigl, M., Nelson, S. & Chklovskii, D. B. Highly nonrandom features of synaptic connectivity in local cortical circuits. *PLoS Biol.* **3**, e68 (2005).
50. Ko, H. *et al.* Functional specificity of local synaptic connections in neocortical networks. *Nature* **473**, 87–91 (2011).

Supplementary Information is linked to the online version of the paper at www.nature.com/nature.

Acknowledgements We thank D. Dombeck for assistance with imaging methods and analysis; C. Dominisoru, M. de Bettencourt, C. Brody and A. Miri for discussions; and M. Goldman, J. Hopfield, D. Aronov, B. Scott and T. Hanks for comments on the manuscript. This work was supported by the NIH (R01-MH083686; RC1-NS068148), a fellowship from the Helen Hay Whitney Foundation (C.D.H.), and a Burroughs Wellcome Fund Career Award at the Scientific Interface (C.D.H.).

Author Contributions C.D.H. performed experiments with assistance from P.C. on the retrograde tracing experiments; D.W.T. implemented the imaging instrumentation; C.D.H. analysed the data with strategy and methods contributions from D.W.T.; C.D.H. and D.W.T. wrote the paper.

Author Information Reprints and permissions information is available at www.nature.com/reprints. The authors declare no competing financial interests. Readers are welcome to comment on the online version of this article at www.nature.com/nature. Correspondence and requests for materials should be addressed to C.D.H. (christopher_harvey@hms.harvard.edu) or D.W.T. (dwtank@princeton.edu).

Methods

Virtual reality system

Experiments were performed using a virtual reality system that has been described previously¹⁰. In brief, head-restrained mice were positioned on top of an air-supported spherical treadmill (8-inch diameter Styrofoam ball; Floracraft)¹¹. The spherical treadmill was surrounded by a toroidal screen onto which a visual virtual environment was projected via a digital light processing projector (Mitsubishi HC3000) and an angular amplification mirror^{10,51-52}. Water rewards were controlled using a solenoid valve (NResearch) and delivered through a feeding tube (Popper and Sons) positioned in front of the mouse's mouth. Rotations of the spherical treadmill were measured using an optical computer mouse (Logitech MX518) positioned at the equator of the Styrofoam ball. The rotational velocity around the horizontal axis perpendicular to the mouse's body axis was used to control forward and backward movements in the virtual environment. The rotational velocity around the vertical axis was used to change the view angle in the environment. The length of a virtual environment was measured as the number of rotations of the treadmill around the horizontal axis required to move from one end of the environment to the other multiplied by the circumference of the Styrofoam ball. The gain factor for view angle changes was set so that 2.5 rotations of the treadmill around the vertical axis caused one full rotation in the virtual environment. The virtual reality software was based on modifications to the Quake2 video game engine (id software) and included real time output signals of the animal's position and view angle and the time of rewards. Virtual environments were designed using a game editor (Quark, <http://quark.planetquake.gamespy.com>). Behavioral data were digitized using a Digidata 1440A and recorded in Clampex software (Molecular Devices). The recorded behavioral parameters were the mouse's location in the virtual environment, the mouse's view angle in the environment, the control signal to the solenoid valve for water rewards, and the spherical treadmill rotational velocity signals.

Behavioral training

All experimental procedures were approved by the Princeton University Institutional Animal Care and Use Committee. C57BL/6J male mice (Jackson Labs) that were 8-12 weeks old prior to the start of behavioral training were used for all experiments. For each mouse before training, a surgery (isoflurane anesthesia) was performed to affix a titanium head-plate for head-restraint to the skull of the mouse using dental cement (Metabond, Parkell). At least one day after head-plate implantation, mice were placed on a water schedule in which they received 1 mL of water per day (total amount, including rewards). Each mouse's body weight was checked daily to ensure that it was $\geq \sim 80\%$ of the pre-water-restriction weight.

Following at least 5 days of water restriction, behavioral training began. Behavioral sessions were performed daily and lasted 45 minutes. Mice were trained to perform the memory-guided T-maze choice task using a sequence of six mazes (Supplementary Fig. 1). Mazes A-C taught the mouse to associate visual cues with a reward; these mazes differed in length and locations of the cues. Mazes D-F taught the mouse to perform a memory-guided task; these mazes differed in total length and length of the delay period. In the final maze, the total length was ~ 310 cm and the length of the delay period was ~ 175 cm. Due to the 270 degree horizontal coverage of the toroidal screen, ~ 5 cm of the maze was projected behind the mouse. The general design of each maze was the same. Each maze consisted of short proximal walls and tall distal walls containing patterns. The width of a corridor in the maze was effectively ~ 1 cm (i.e. the distance the mouse could actually move transversely between proximal walls). There were two variants of each maze that had different visual cues. The visual cue was either white proximal walls with black dots and a tall white distal wall positioned on the left side of the track or green proximal walls with black dots and a tall green distal wall positioned on the right side of the track (Supplementary Fig. 1c). The two variants of each maze differed only in the visual cue and the position on the track at which a reward was given (i.e. left or right arm of the T); all other parts of the track were identical between variants of each maze. We note that the green cue was likely perceived by the mouse as a middle gray tone. Mice have two sets of cones that can detect ultraviolet light and green light⁵³; however, our digital light processing projector did not emit ultraviolet light.

On each trial, the mouse was positioned at the beginning of the maze. The mouse then had to run down the stem of the T and make a turn, either to the left or to the right depending on

the visual cue, by spinning the spherical treadmill around its vertical axis to cause a change in view angle. If the mouse made the correct turn and moved ~25 cm down the appropriate arm, a small water reward (4 μ L) was given and there was a brief inter-trial interval (~3 s long) in which the visual display was black. If the mouse made the incorrect turn, the reward was omitted and the inter-trial interval was longer (~6 s). After the inter-trial interval the mouse was positioned back at the start of the maze by teleportation in virtual reality, and a visual cue that indicated the turn direction for a reward was selected randomly. The delay period was included as a section of the maze in which the mouse had to run straight down the stem of the T while remembering the identity of the cue. Mice completed trials at a mean rate of 3.3 ± 0.5 trials per minute.

Behavioral training began on Maze A. Mice were advanced to subsequent mazes in the training sequence once they achieved either greater than 3 rewards per minute on average or greater than 70% correct on two consecutive sessions. If after advancing to a new maze behavioral performance decreased, mice were in some cases returned to an earlier maze in the sequence for additional training (33% of mice; Supplementary Fig. 1d, middle). These decreases in performance most often occurred with the introduction of the delay period. The average time to reach a performance of > 70% correct on Maze F was 34 training sessions (range: 26-44 sessions).

Imaging

Upon reaching proficiency on Mazes A-D in the training sequence (Supplementary Fig. 1), mice underwent surgery (isoflurane anesthesia) for virus injections and implantation of imaging windows and head-plates. The head-plate used for behavioral training was removed. A 3-mm diameter craniotomy centered over the PPC was made using stereotactic coordinates (2 mm caudal, 1.7 mm lateral to bregma; left hemisphere). Three injections (~30 nL per injection over ~2 minutes; ~200 μ m apart) of a solution containing AAV2/1-*synapsin-1-GCaMP3* virus³⁵ (obtained from the University of Pennsylvania Vector Core Facility) were made at the center of the craniotomy and ~275 μ m beneath the surface of the dura. Injections were performed using a beveled glass pipette (~10-20 μ m tip) and a custom air pressure injection system. The pipette was advanced into the brain, using a micromanipulator (Sutter MP285), at a 30 degree angle relative to the horizontal to minimize compression of the brain as the pipette passed through the

dura. For 2 days prior to surgery, mice received 5 mL of water per day because viral transduction efficiency was low in water-restricted mice. In the same surgery, a two-piece titanium head-plate and window were then implanted for chronic imaging, as described previously⁵⁴. The window consisted of a uniform thickness silicone elastomer plug (3-mm diameter, 0.65-mm thickness; made from Kwik-Sil, World Precision Instruments) bonded to a #1 thickness, 3.5-mm diameter coverslip (custom made from Erie Scientific, Thermo Scientific) using a custom mold. The head-plate was affixed to the skull using opaque dental cement (Metabond mixed with ~5% vol/vol India ink) to prevent light leakage from the virtual reality display into the microscope. A titanium ring, which interfaced with an aluminum ring and black rubber surrounding the microscope objective, was cemented to the top of the head-plate for fluorescence isolation¹² (see below). At least one day after surgery, mice resumed behavioral training, starting with Maze D. GCaMP3 expression reached fairly stable levels after ~14 days of expression, at which point mice had become proficient at Maze F. Imaging experiments began at least 14 days following virus injection and were carried out for up to 6 weeks after virus injection. GCaMP3 expression appeared stable for at least 6 weeks post injection. After that point in some cases, bright cells with GCaMP3 present in their nuclei were observed, as noted previously^{12,35}. These cells had long duration Ca^{2+} transients that were rarely correlated to the task. Imaging data were not included if these cells were present in the field-of-view.

Imaging was performed using a custom two-photon microscope that has been described previously¹². In brief, the microscope was designed to isolate the collection of photons emitted by fluorescent probes in the brain from the bright visual display for the virtual reality system. The internal optics of the microscope were enclosed in a light-tight aluminum shell, except for one hole for the microscope objective and one hole for laser light entry. A colored glass filter (780 nm long-pass; Thorlabs) was placed at the laser entry point to allow entry of the laser excitation light but to prevent entry of light from the projection system. A piece of black rubber was attached around the objective with an aluminum ring at the sample end of the objective. This aluminum ring fit around the outside of the titanium ring cemented to the mouse's head-plate, creating a light-tight barrier to prevent the entry of light from the projection system into the microscope through the objective.

The Ti:sapphire excitation laser (Chameleon Ultra II, Coherent) was operated at 920 nm (< 80 mW average power at the sample). GCaMP3 fluorescence was isolated using a bandpass

filter (542/50, Semrock) and detected using a GaAsP photomultiplier tube (1077P-40, Hamamatsu). Microscope control and image acquisition were performed using ScanImage⁵⁵ (version 3.6). Images were acquired at 15.6 Hz at a resolution of 256 x 64 pixels (~300 x 150 μm field-of-view). Imaging and behavioral data were synchronized by simultaneously recording the command signal to the slow axis galvanometer and behavioral data at a sampling rate of 1 kHz using the Digidata/Clampex acquisition system. Time-series acquisitions were collected in sets of 5000 frames with a 2-3 minute gap between acquisitions. A total of up to 30,000 frames were collected from a single field-of-view during a single behavioral session. Major out of plane drift (z direction) was not observed over this length of time; the position of the microscope was not adjusted during the full length of the time-series acquisition. Photo-bleaching was observed at a rate of ~1% per minute. Different fields-of-view in the same mouse were imaged on different sessions. Data were analyzed from 29 fields-of-view from 6 mice.

Electrophysiology

Procedures for electrophysiology experiments (Supplementary Fig. 10) followed a similar time course to those for imaging with several differences. During the implantation of the head-plate for behavioral training, the position of the PPC on both the left and right hemispheres was marked on the skull using stereotaxic coordinates. Behavioral training continued through the sequence of mazes (Maze A to Maze F; Supplementary Fig. 1) until the mouse was proficient at Maze F. Then a small craniotomy (~0.5-0.75 mm diameter) was made at a position 0.5 mm caudal to the PPC site (i.e. 2.5 mm caudal, 1.7 mm lateral to bregma). The craniotomy was made caudal to the PPC because the electrode was inserted moving caudal to rostral at an angle of 30 degrees relative to the horizontal; this orientation allowed the electrode to hit the rostral-caudal center of the PPC at a depth of ~250 μm beneath the dura. Recordings were performed from each hemisphere for up to 3 days. The craniotomy was covered with silicone elastomer (Kwik-Sil) between recording sessions.

Extracellular recordings were performed with a glass electrode filled with 0.5 M NaCl (~2.5 $M\Omega$ pipette resistance) and mounted on a micromanipulator (Sutter MP285) positioned behind the mouse. The reference electrode was positioned outside the craniotomy in extracellular saline containing (in mM): 150 NaCl, 2.5 KCl, 10 HEPES, pH 7.4. Signals were amplified (Dagan BVC-700A), electronically filtered between 5 Hz and 10 kHz (Brown-Lee Model 440),

and digitized at 20 kHz along with behavioral signals (Molecular Devices Digidata 1440A). Recordings were made at depths of between 150 and 350 μm beneath the surface of the dura. The Styrofoam ball was washed in a benzalkonium chloride solution (Benz-all) to reduce low frequency (< 50 Hz) electrical noise caused by ball rotation, possibly due to charge buildup on the ball; this solution also served to disinfect the ball. Recordings were performed from 3 mice; task-modulated and choice-specific cells were identified in all 3 mice.

Spikes were sorted offline using an amplitude threshold from band-pass filtered versions of the recording (filtered from 300 Hz to 10 kHz using a finite impulse response filter). At most one unit was isolated from a single recording. Spike waveforms were overlaid and visually inspected to help verify single unit recordings. Interspike interval distributions were plotted to make sure no spikes fell within the refractory period (< 2 ms). Firing rates were calculated using the total number of spikes occurring in a 50 ms bin. To generate predicted fluorescence traces from electrophysiology data (Supplementary Fig. 11), spikes were first binned into 64 ms time bins (i.e. the duration of a single imaging frame). The binned spike counts were changed into peak $\Delta\text{F/F}$ values using the spike number-to- $\Delta\text{F/F}$ relationships in Figure 6c of ref. 35. The resulting trace was convolved with a calcium impulse response function (rise time: $t_{1/2} = 52$ ms, decay time: $t_{1/2} = 384$ ms).

The electrophysiological recordings corroborated our imaging results. First, we identified cells based on electrically-recorded spikes that had similar temporal profiles to those imaged with GCaMP3, including cells active during the cue, delay, and turn periods of the task (Supplementary Fig. 10). These cells had different temporal profiles during the task relative to one another (Supplementary Fig. 10c), which is consistent with the sequential activation we observed from our imaging data. Also, convolving a spike train with a calcium impulse response function was able to create a $\Delta\text{F/F}$ trace similar to those we obtained from imaging (Supplementary Fig. 11), indicating that spikes alone can likely account for the Ca^{2+} concentration increases in our imaging experiments. Also, previous work showing the quantitative relationship between spiking and changes in fluorescence intensity for GCaMP3 in layer 2/3 cortical neurons further indicates that the fluorescence changes we observed were likely to be exclusively, or in large part, triggered by changes in spiking activity³⁵.

Retrograde and anterograde tracing experiments

To identify the anatomical location of the PPC, retrogradely-transported red fluorescent beads⁵⁶ (Lumafluor) were injected using stereotaxic coordinates through a small craniotomy (~0.5 mm diameter; Supplementary Fig. 4a-c). Beads were injected using a glass pipette with a broken, beveled tip (~10 µm diameter tip) at three depths beneath the dura (200, 450, 700 µm). Injections were typically 50 nL but in some cases varied up to ~150 nL. Forty-eight hours after the injection, the brain was removed and placed in 4% paraformaldehyde for ~24 hours. Coronal slices (150 µm thick) were cut using a vibrating slicer (Vibratome Model 1500) and imaged with an epifluorescence stereomicroscope (Leica MZ16FA). The identities of the labeled regions were determined using a mouse brain atlas⁵⁷.

For anterograde tracing, injections of AAV serotype 2/1 containing GCaMP3 or GFP under the human synapsin promoter were performed using stereotaxic coordinates through a small craniotomy (~0.5 mm diameter; Supplementary Fig. 4d-g). One or two injections of ~30 nL each were performed at a depth of ~275 µm beneath the dura. Three to ten weeks after the viral injection the brain was removed, fixed in 4% paraformaldehyde, and sliced into 150 µm-thick coronal sections. Sections were imaged using an epifluorescence stereomicroscope. We did not detect labeled cell bodies in regions a long distance from the injection site, including following two-photon imaging of a subset of the fixed sections; retrograde labeling following infection of axons was therefore infrequent.

Inactivation experiments with muscimol

To test whether the PPC was necessary for the behavioral task, bilateral injections of muscimol (Sigma) were performed on mice proficient at performing the memory-guided task (Fig. 1d-e). Injections (50 nL, 1 ng/nL, in extracellular saline (described above); ~350 µm beneath the dura) were made with a beveled glass pipette through a small (0.5 mm diameter) craniotomy on each hemisphere. The pipette was inserted into the brain at a 30 degree angle relative to the horizontal, as in the electrophysiology experiments. Injections were performed in awake mice running on the spherical treadmill. Following the injection of muscimol, mice were returned to their home cage for two hours before behavioral testing. Sessions with no injections or saline injections (50 nL) followed the same time course as during muscimol injections. One behavioral session was performed per day. Following multiple sessions on the memory-guided

task with interleaved injection conditions (Fig. 1d), mice were then switched to a visually-guided form of the task. The maze for this task had the same dimensions, but contained a visual cue (a tall distal wall) located at the reward site and visible throughout the task (Supplementary Fig. 1b).

We chose the amount of muscimol to inject based on previous studies that performed electrical recordings in rat cortex at various distances from the injection site to measure the spread of the inactivation⁵⁸. In rat cortex, the amount of muscimol we injected is expected to have an effect over a distance similar to the size of the mouse PPC. Also, previous studies in mouse cortex in which higher concentrations and volumes of muscimol were injected^{32,59} suggest that the behavioral effect of the spread of inactivation is likely within the dimensions of the mouse PPC. We did not observe any major motor deficiencies following muscimol injection.

Linear track behavior

Mice were trained to perform a task in a 1.8 m-long linear track using methods described previously¹⁰. In brief, mice ran to one end of the track to receive a water reward and then had to run to the opposite end to receive the next reward; two consecutive rewards were not available at a single reward site. The linear track was identical to the one used in previous studies of CA1 cells in the hippocampus^{10,12}, except that the pattern on the middle portion of the track was black walls with white crosses. The three segments of the track had proximal wall patterns identical to those used in the T-maze: black walls with white dots, black walls with white crosses, and white walls with black dots. The short dimension of the maze was identical to the short dimension of the T-maze (~9 cm with ~1 cm of permitted lateral movement). Mice trained on the linear track received rewards at rates similar to those used for place cell recordings on the linear track (> 3 rewards per minute on average). Surgical preparations, imaging, and the extraction of ΔF/F time series were performed using the same methods as for the T-maze task.

Open-loop T-maze

In the open-loop experiments, movies of simulated runs through the T-maze were played to mice that passively viewed the visual scenes. The control signals from the optical computer mouse (measuring the rotational velocities of the treadmill) were not used. Instead voltages for translation and view angle changes were generated by a function generator and input as the

control signals in the virtual reality software. On each trial, the translation signal was a square pulse with a duration of 9 s. The signal for view angle changes was a positive-going (for right trials) or a negative-going (for left trials) square pulse with duration of 1.5 s starting after a 7.5 s delay. The amplitudes and shape of the signals approximately matched those used during mouse-driven trials. The speed of progression through the maze therefore closely approximated movement through the maze in the closed-loop experiments. These signals triggered a run down the stem of the T followed by a left or right turn at the T-intersection, as occurs in the closed-loop trials. Simulated left and right turn trials were played in random order. In some cases the air support for the spherical treadmill was present (so the mouse could run and move, without an effect on the virtual environment), and in other cases the air support was turned off (so that the mouse could not rotate the treadmill); no obvious differences between these cases were observed. The PPC was imaged during the open-loop trials in mice that were not trained on the T-maze task. Surgical preparations, imaging, and data analysis were performed using the same methods as for the closed-loop T-maze task.

Data analysis

All analysis was performed using toolboxes and custom code in Matlab (Mathworks). All data are presented as mean \pm standard deviation unless noted otherwise.

Only behavioral trials that were complete (i.e. the mouse ran the full length of the maze) and in which the mouse did not turn around in the maze (i.e. running only toward the stem of the T followed by one turn) were analyzed. For each trial, different time points in the trial were defined to establish trial periods corresponding to the stimulus (cue), delay, and response (turn). The trial start point was defined as the time when the maze became visible, and the trial end point was defined as the point when the maze was made no longer visible. The trial ended immediately after the mouse reached the rewarded position in the track on correct trials or the same location in the opposite arm on error trials. The time between the end of one trial and the start of the next trial was defined as the inter-trial interval (~3 s for correct trials, ~6 s for error trials). The cue offset was defined as the time at which the mouse moved past the tall distal wall and out of the region with green or white proximal walls; this was the last point in the trial at which visual information about the location of the reward was present. The cue period was defined as the time between the trial start and the cue offset; the visual cues were present and

visible throughout the duration of the cue period. The turn onset was defined as the last time point when the mouse was in the stem of the T between the visual cues and the T-intersection (i.e. black walls with white crosses; Fig. 1a) and when the rotational speed of the spherical treadmill around the vertical axis (i.e. for view angle changes) was below a threshold value (0.04 rev/s; Fig. 1c). To effectively run down the long narrow stem of the T-maze, the treadmill rotational speed about the vertical axis needed to be small or else the mouse would have turned around and not reached the T-intersection. In contrast, to execute a turn at the T-intersection, a large change in view angle was necessary and thus a large increase in the rotational speed of the treadmill about the vertical axis was required. Therefore, defining the turn onset based on rotation of the treadmill was an effective method. Also, examination of treadmill rotational velocity on single trials illustrates that this definition effectively defined the time at which the rotational velocities began to differ between right and left turn trials (Fig. 1c, Supplementary Fig. 3a-b). The turn onset often occurred before the T-intersection was reached but was in general close to the T-intersection (distance to intersection: 22.0 ± 18.5 cm, distance to visual cue: 153.6 ± 18.5 cm). The delay period was defined as the time between the cue offset and turn onset. The turn period was defined as the time between the turn onset and the end of the trial. In some of the behavioral sessions during imaging (31%), the view angle and treadmill rotation about the vertical axis were significantly different between right and left choice trials during the delay period (two-tailed t-test, significance level of $p < 0.01$). This difference was due to a small fraction of trials in which the mouse oriented its view toward the upcoming turn direction and began turning slightly during the delay period. To eliminate these trials, thresholds for the mean view angle and the mean treadmill rotation during the delay period were introduced; mean values for the view angle and rotation had to be below these threshold values for an individual trial to be included in the analyzed data. The thresholds were reduced, eliminating more and more trials, until the view angle and treadmill rotation did not differ significantly during the delay period before right and left turns. For those sessions in which trials had to be eliminated to meet these criteria, an average of 21% of trials had to be eliminated. The total fraction of eliminated trials across all sessions was $< 7\%$.

Imaging time-series from the same field-of-view that were acquired during the same behavioral session (5000 frames per series, 15,000-30,000 frames per field-of-view) were concatenated. Because the ending fluorescence level in one time-series differed from the starting

fluorescence in the subsequent time-series (e.g. due to recovery from photo-bleaching by diffusion), during concatenation the fluorescence values in the following time-series were adjusted such that the mean whole-field fluorescence averaged over the first 300 frames of the following time-series was equal to the mean whole-field fluorescence averaged over the last 300 frames of the previous time-series. A single scale factor was used to adjust all frames in the following time-series. This created smooth transitions between concatenated series, which was helpful for motion correction. Only complete behavioral trials were analyzed, so small, spurious fluorescence changes introduced at the boundaries between individual series by the concatenation were not considered as possible Ca^{2+} transients during subsequent analysis. Following concatenation, the entire time-series was motion corrected using a whole-frame cross correlation method⁶⁰.

Regions-of-interest (ROI) for putative cells were selected manually (Fig. 2a). All the pixels inside the ROI were averaged to obtain a time-series fluorescence trace for each ROI. Slow timescale changes in the fluorescence traces (e.g. due to photo-bleaching or small drift in the z focal position) were removed by determining the distribution of fluorescence values in a ~20-s interval (i.e. much longer than the duration of a Ca^{2+} transient) around each sample time point and subtracting the 8th percentile value¹¹. The baseline-subtracted fluorescence traces for each ROI were then analyzed for the ratio of positive- to negative-going transients of various amplitudes and durations, as described previously¹¹. This analysis is based on the idea that increases in neural activity are expected to trigger only increases in fluorescence, whereas motion-induced fluorescence changes are expected to be observed as both fluorescence intensity increases and decreases. By finding increases in fluorescence intensity of bigger amplitude and longer duration than the negative-going transients, one can isolate transients that are unlikely to be due to brain motion. We used this analysis to identify significant transients with less than a 5% expected false positive rate and generated significant transient-only traces that were used for all subsequent analysis, except the factor analysis (Fig. 4). Note that in the significant transient-only traces the significant transients were unmodified, and the values at time points between significant transients were set to zero.

$\Delta F/F$ traces were time aligned using methods that depended on the analysis performed. In most analyses, fixed duration segments of individual trials were aligned to the cue offset, the turn onset, and the trial end. Multiple alignment points were used because trials differed in duration,

and including more alignment points allowed for better comparisons of behaviorally-similar time points across trials and across cells. For this alignment method, only trials that had a cue period longer than 3 s, a delay period longer than 3 s, and a turn period longer than 2 s were included (80% of trials). Note that this alignment method introduced gaps in the data. For analyses in which data without gaps were necessary, data from each trial were aligned to the cue offset only. Unless noted otherwise, all analyses were performed using only the correct trials and excluding the error trials.

Each ROI, selected as a putative cell body, was classified as either active or not active. Active cells had greater than 2 significant transients per minute on average over the entire imaging time. Note that nearly all the imaged cells showed significant Ca^{2+} transients during the behavioral session (96% of cells had > 0.2 transients per minute). Of the highly active cells, cells were classified as either task-modulated or non-task-modulated cells based on if they had a prolonged period of increased activity in their mean $\Delta F/F$ trace averaged across all correct trials, aligned to the cue offset (Supplementary Fig. 5). First, putative time periods of increased activity were identified as stretches of at least 20 consecutive time points (~ 1.3 s), occurring at any time during the trial or inter-trial interval, in which the $\Delta F/F$ values for the consecutive time points were all greater than 0.25 times the maximum $\Delta F/F$ value in the mean trace. A cell was considered to be a task-modulated cell if it had at least one such time period and if the mean $\Delta F/F$ during this time period was greater than 3 times the mean $\Delta F/F$ at all time points outside the putative times of increased activity. 93% of task-modulated cells had one time period of increased activity, 7% had two periods, and $< 1\%$ had three periods. Of the task-modulated cells, cells were classified as distinguishing the trial type if they had significantly different $\Delta F/F$ values on correct right and correct left trials during the time period of increased $\Delta F/F$ values (determined by a two-tailed t-test with significance value set at $p < 0.01$). The level of trial-type selectivity was quantified by a value equal to $(\text{mean } \Delta F/F_{\text{right trials}} - \text{mean } \Delta F/F_{\text{left trials}}) / (\text{mean } \Delta F/F_{\text{right trials}} + \text{mean } \Delta F/F_{\text{left trials}})$. Cells distinguishing the trial type that had a selectivity index greater than zero were considered right-preferring cells and those that had a selectivity index less than zero were considered left-preferring cells. For some analyses, right- and left-preferring cells were classified by a trial period preference. Trial period preference was defined based on a histogram of the times of the center-of-mass of the mean $\Delta F/F$ trace, averaged across all correct trials aligned to the cue offset, turn onset, and trial end, excluding gaps (t_{COM} ; Fig. 3a).

Population data were compared to shuffled versions of the dataset to verify that the sequences were not an artifact of ordering the data (Supplementary Figs. 14, 17, 18). Shuffled versions of each cell's $\Delta F/F$ trace were created by rotating the $\Delta F/F$ time series (each data point was from a single imaging frame, 64 ms/frame) by a random amount relative the position values in the maze. To quantitatively compare the unshuffled and shuffled data, a ridge-to-background ratio was calculated for each cell from that cell's mean $\Delta F/F$ trace. The ridge was defined as the mean $\Delta F/F$ in the 20 bins (64 ms/bin in temporal analyses or 2.25 cm/bin in spatial analyses) surrounding the peak value, and the background was defined as the mean $\Delta F/F$ in all the other data points. We note that ordering the data by the timing of the peak is expected to create a ridge of activity along the diagonal. The relevant comparison is therefore between the ordered unshuffled data and the ordered shuffled data, which accounts for the effects of ordering the data by peak time.

Correlation coefficients were from Pearson's correlations, unless noted otherwise. Correlations were calculated using the unaveraged $\Delta F/F$ traces, in which each data point corresponded to a single imaging frame (e.g. 30,000 imaging frames, 64 ms/frame). Correlations for $\Delta F/F$ traces outside the preferred epoch were calculated excluding time points in the preferred behavioral period and excluding time points that contained a significant transient that extended into the preferred period. All calculations based on anatomical distances between cells (Fig. 5) excluded cell pairs with centroids located less than 15 μm from each other to rule out the possibility of intermixed signals between neighboring cells.

Principal component analysis (PCA; Fig. 3b, Supplementary Fig. 15) was performed using Matlab toolboxes. PCA was performed on the mean $\Delta F/F$ traces for a specified set of neurons using an m neurons by n time points dataset (e.g. 404 neurons by 168 time points in Fig. 2d). Mean $\Delta F/F$ traces were normalized to the peak value in the mean trace for each neuron before performing PCA. In Fig. 3b, the first two principal components captured 61% of the variance.

Factor analysis (Fig. 4) with 15 common factors was performed using Matlab toolboxes and custom code. Factor analysis was performed using all time points for all ROIs from individual imaging sessions. $\Delta F/F$ data between significant transients were not set to zero. $\Delta F/F$ traces were smoothed over a 30-frame window using a moving average. Data were organized into an m time points by n ROIs dataset (e.g. 30,000 time points by 76 ROIs in Fig. 4a). Factor

analysis was used instead of PCA because factor analysis better embodies shared fluctuations in activity across the population and more effectively discards independent variability specific to individual neurons. Distances between trajectories were measured as Euclidean distances between corresponding time points. The trajectory selectivity index was a measure of how similar individual trajectories were to the mean trajectories for correct right and left trials, based on distance measurements (d), and was defined as: $(d_{\text{to mean traj, opposite choice}} - d_{\text{to mean traj, same choice}})/(d_{\text{to mean traj, same choice}} + d_{\text{to mean traj, opposite choice}})$. For example, for a left choice trial, either correct or incorrect, an index score of 1 means the single trial trajectory was at the same point in state space as the mean correct left choice trajectory, and an index score of -1 means the single trial trajectory was at the same point in state space as the mean correct right choice trajectory. Classification was performed for individual trials based on distances to the mean correct right choice and mean correct left choice trajectories (Supplementary Fig. 19b). If the distance to the mean left trajectory was less than the distance to the mean right trajectory, for example, that time point for that trial was classified as ‘left choice’, and vice versa. Classification accuracy was calculated at each time point by averaging across trials for individual imaging sessions. In all distance measurements and classification, the mean trajectories were calculated excluding the test trajectory (i.e. leave-one-out cross validation). Statistics for classification accuracy (Supplementary Fig. 19c) were performed by shuffling the trial labels (‘right choice’ and ‘left choice’) and performing classification based on the shuffled labels. Shuffling was repeated 1000 times.

To address the contributions of various behavioral parameters to the activity of neurons during the delay period, we used a multiple linear regression analysis (Supplementary Table 1). We considered only those cells that were considered delay-preferring cells based on being choice-specific and task-modulated with a COM of mean $\Delta F/F$ falling in the middle peak of the COM distribution (Fig. 3a, middle green segment). Only time points during the delay period in which the mean $\Delta F/F$ values between right and left correct trials differed significantly were considered for each cell. On each trial, the mean $\Delta F/F$ and the mean values of various behavioral parameters were calculated during these time points. The behavioral parameters were the lateral position in the maze (short dimension), the view angle in the environment, the rotational velocity of the treadmill for translation, and the rotation velocity of the treadmill for view angle changes. First, we considered only the effect of the behavioral choice using $F = \beta_0 + \beta_1 C + \varepsilon$, where F is

the mean $\Delta F/F$, β_0 is a constant coefficient, β_1 is a fitted coefficient, C is the behavioral choice on the trial (0 for left and 1 for right), and ε is an error term. Next, we included all the behavioral parameters using $F = \beta_0 + \beta_1 C + \beta_2 P + \beta_3 V + \beta_4 R_1 + \beta_5 R_2 + \varepsilon$, where P is lateral position, V is the view angle, and R_{1-2} are the rotational velocities of the treadmill. We used the partial F-statistic to determine whether there was a significant effect ($p < 0.05$) of each parameter for each cell.

To compare the activity patterns of PPC neurons during the T-maze task with the responses of PPC neurons during a linear track task and an open-loop play-through of the T-maze (Supplementary Figs. 17-18), we analyzed the spatial modulation of neuronal activity in the virtual environment. We used criteria for spatial modulation that were used previously for GCaMP3 signals in hippocampal place cells¹². First, the mean $\Delta F/F$ in 2.25 cm spatial bins covering the environment was calculated (the T-maze positions were linearized for this analysis). Values were considered separately for the different versions of the T-maze (maze 1 and maze 2) and for the different running directions on the linear track. We identified cell activities that were potentially spatially modulated as those that had at least 5 consecutive spatial bins with (1) a mean $\Delta F/F$ value greater than 0.25 times the peak mean $\Delta F/F$ value across all bins, (2) a mean $\Delta F/F$ value averaged across these bins of greater than 3 times the mean $\Delta F/F$ averaged across all other bins, and (3) a Ca^{2+} transient in at least 20% of the time points spent in these bins of elevated activity. To verify that this increase in activity was statistically significant, we then rotated the $\Delta F/F$ values at each imaging time point (64 ms per time point) by a random amount relative to the position values and asked whether a field of increased activity that met the above-stated 3 criteria was present in the rotated data. A cell was considered to be spatially modulated if it had a field in the unrotated data and fields in less than 5% of the rotated cases (1000 rotations were performed per cell). We also quantified the spatial information content in a neuron's activity pattern as:

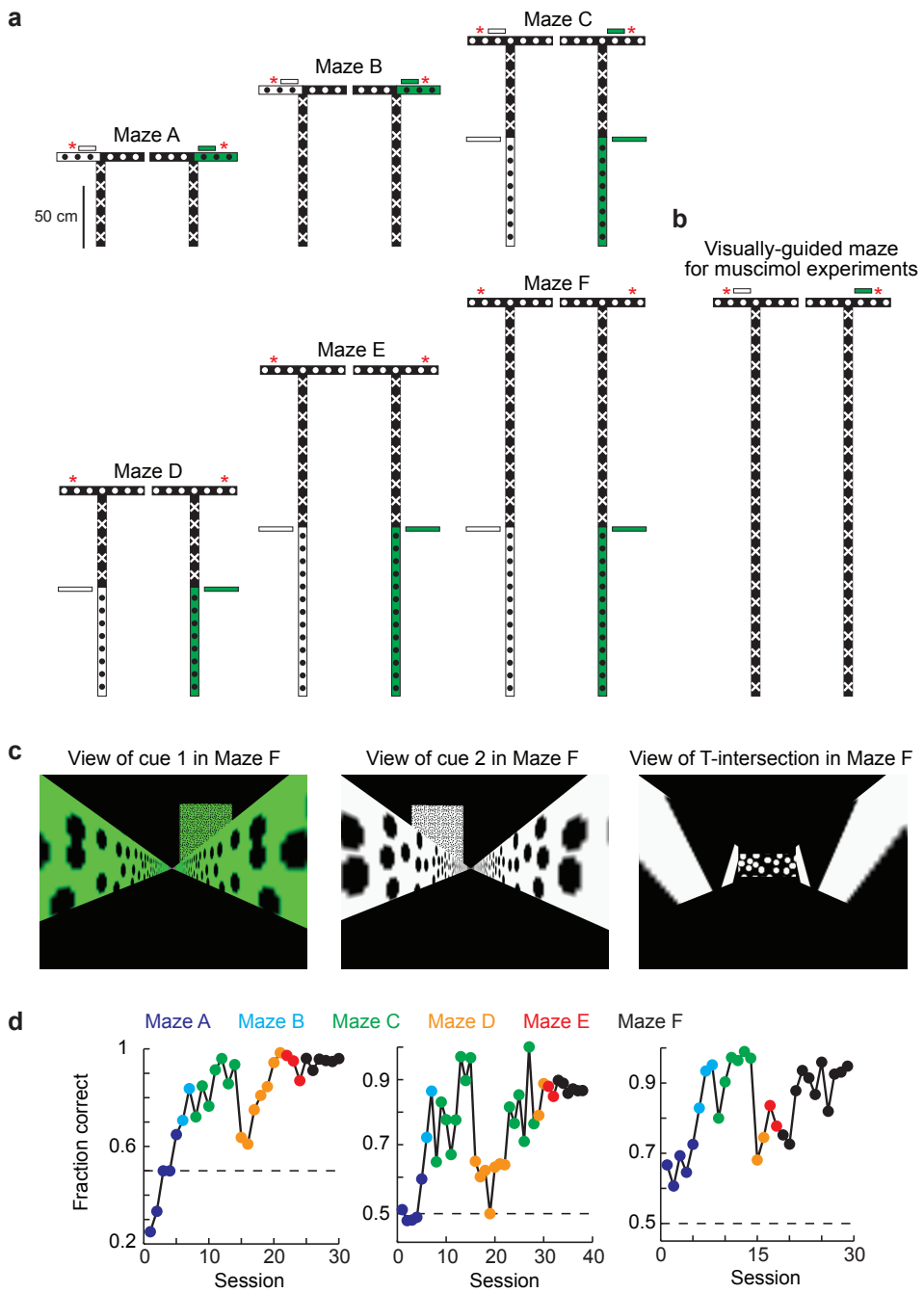
$$\sum p_i(f_{i,\text{unshuffled}}/\langle f_{\text{unshuffled}} \rangle) \log_2(f_{i,\text{unshuffled}}/\langle f_{\text{unshuffled}} \rangle) - \sum p_i(f_{i,\text{shuffled}}/\langle f_{\text{shuffled}} \rangle) \log_2(f_{i,\text{shuffled}}/\langle f_{\text{shuffled}} \rangle)$$

where p_i is the fraction of the trial time spent in the i th spatial bin (2.25 cm bin width), f_i is the mean $\Delta F/F$ in the i th bin and $\langle f \rangle$ is the mean $\Delta F/F$ across all bins. A value was obtained for the unshuffled data and from this value the mean value from 100 shuffled versions was subtracted. Shuffling was performed by rotating the $\Delta F/F$ time series (64 ms/frame sampling) by a random

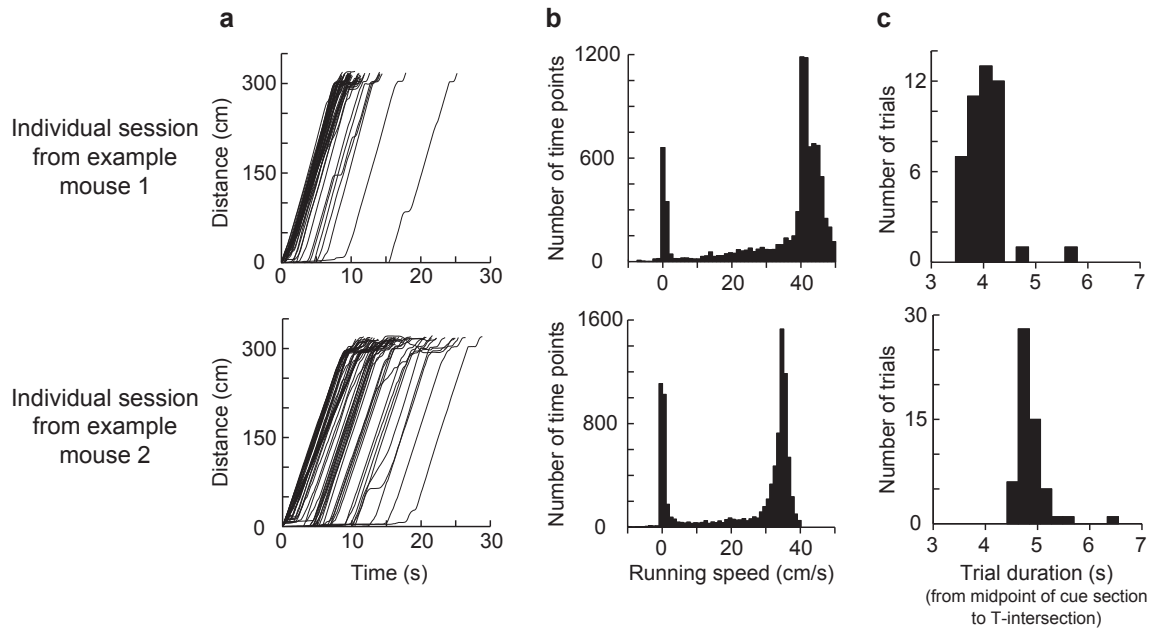
amount relative to the position values. A cell was considered to have location-specific activity if the information content in the unshuffled data was higher than > 95% of the shuffled values.

References (continued)

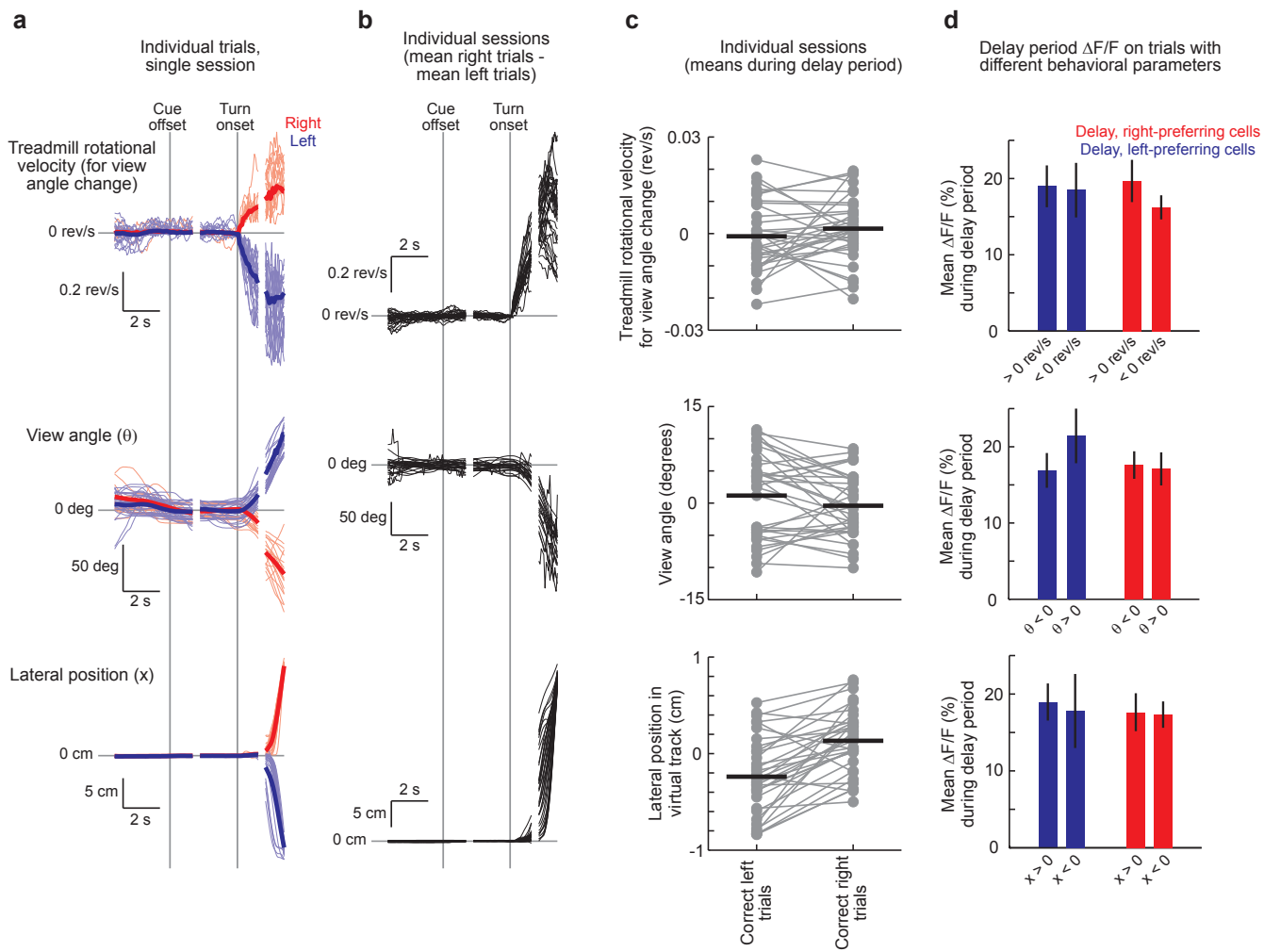
- 51 Holscher, C., Schnee, A., Dahmen, H., Setia, L. & Mallot, H. A. Rats are able to navigate in virtual environments. *J Exp Biol* **208**, 561-569 (2005).
- 52 Chahl, J. S. & Srinivasan, M. V. Reflective surfaces for panoramic imaging. *Appl Opt* **36**, 8275-8285 (1997).
- 53 Jacobs, G. H. The distribution and nature of colour vision among the mammals. *Biol Rev Camb Philos Soc* **68**, 413-471 (1993).
- 54 Dombeck, D. A., Graziano, M. S. & Tank, D. W. Functional clustering of neurons in motor cortex determined by cellular resolution imaging in awake behaving mice. *J Neurosci* **29**, 13751-13760 (2009).
- 55 Pologruto, T. A., Sabatini, B. L. & Svoboda, K. ScanImage: flexible software for operating laser scanning microscopes. *Biomed. Eng. Online* **2** (2003).
- 56 Katz, L. C., Burkhalter, A. & Dreyer, W. J. Fluorescent latex microspheres as a retrograde neuronal marker for in vivo and in vitro studies of visual cortex. *Nature* **310**, 498-500 (1984).
- 57 Paxinos, G. & Franklin, K. *The Mouse Brain in Stereotaxic Coordinates*. 2nd edn, (Academic Press, 2001).
- 58 Krupa, D. J., Ghazanfar, A. A. & Nicolelis, M. A. Immediate thalamic sensory plasticity depends on corticothalamic feedback. *Proc Natl Acad Sci U S A* **96**, 8200-8205 (1999).
- 59 O'Connor, D. H. *et al.* Vibrissa-based object localization in head-fixed mice. *J Neurosci* **30**, 1947-1967 (2010).
- 60 Miri, A., Daie, K., Burdine, R. D., Aksay, E. & Tank, D. W. Regression-based identification of behavior-encoding neurons during large-scale optical imaging of neural activity at cellular resolution. *J Neurophysiol* **105**, 964-980 (2011).



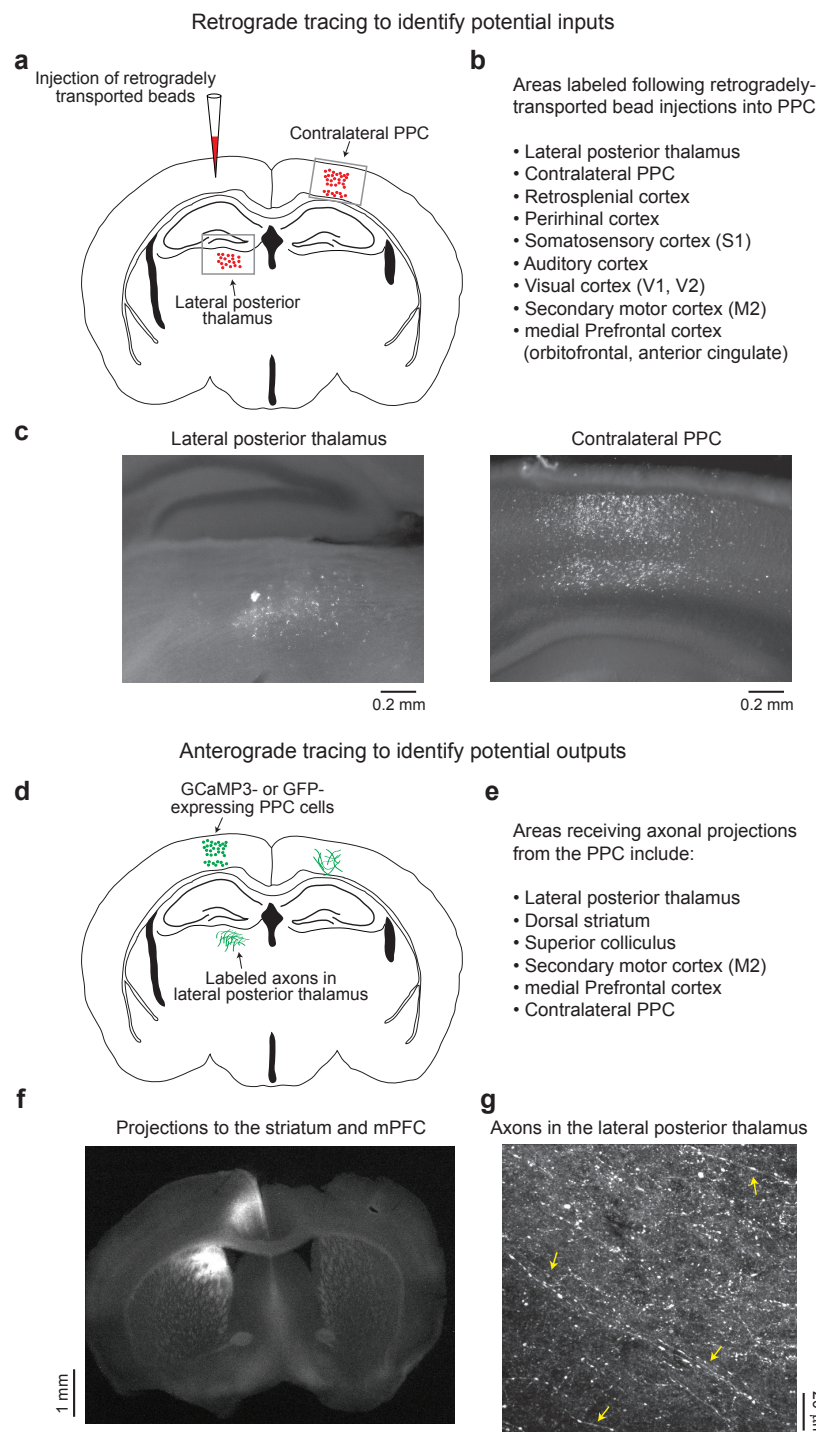
Supplementary Figure 1 | Behavioral training and maze designs. **a**, Sequence of mazes used for behavioral training. Two versions of each maze are shown to illustrate the visual cue variants. Red asterisks mark the reward location. **b**, Schematic of the maze for the visually-guided task used during some muscimol experiments (Fig. 1e). **c**, Screen captures of the virtual environment. **d**, Behavioral performance for three example mice across training sessions (one session per day).



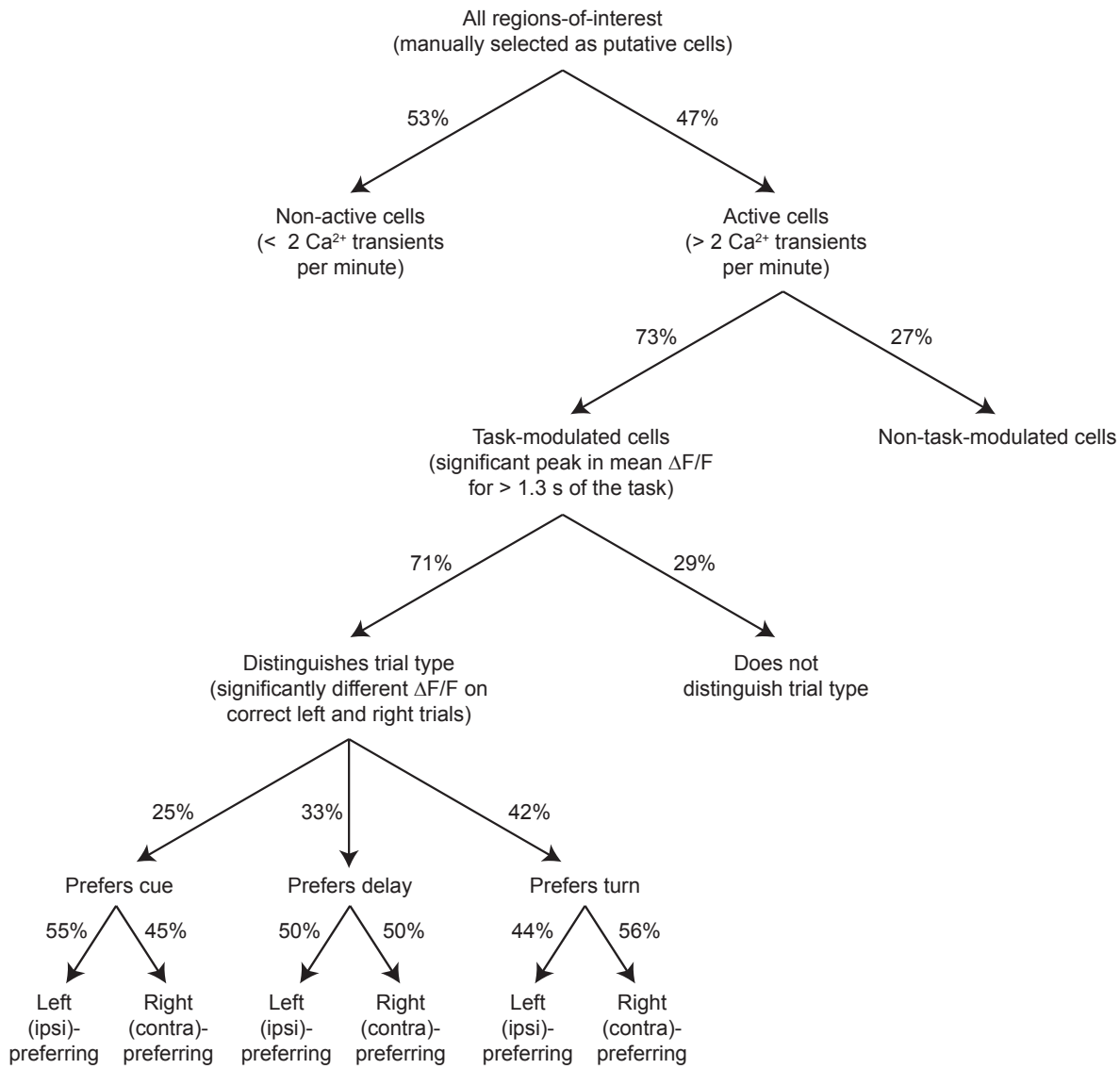
Supplementary Figure 2 | Mouse running speeds. **a**, Example plots of distance traversed through the maze as a function of time. Each line is an individual trial. Two representative example mice are shown. Note the consistent running speed (slope) across trials. The variability in trial duration most frequently resulted from a period of waiting at the beginning of the trial. **b**, Histogram of the running speed calculated over individual 0.5 s periods. **c**, Histogram of trial durations from the midpoint of the cue section of the maze to the T-intersection. The full trial duration was more variable due to differences in waiting at the beginning of the trial, as shown in (a).



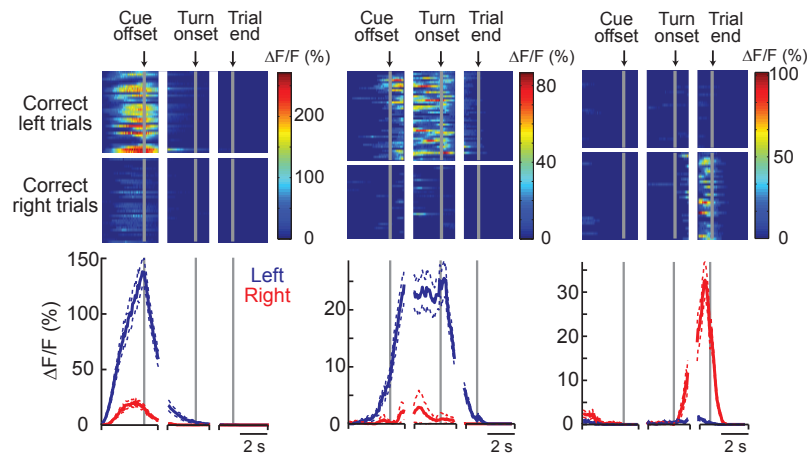
Supplementary Figure 3 | Behavioral parameters during the task. **a**, Treadmill rotational velocity for view angle changes (top panel), view angle (θ , middle), and lateral position along the short dimension (x, bottom) for individual correct right (red) and left (blue) choice trials in a single session. Thick lines indicate the mean. **b**, The same behavioral parameters as in (a) summarized for individual sessions as the mean values on right choice trials minus the mean values on left choice trials at each time point. **c**, Mean values for each parameter during the delay period on individual sessions. Each set of connected dots is one session. Horizontal lines indicate the mean. Rotational velocity: $p > 0.25$, view angle: $p > 0.15$, lateral position: $p < 0.01$ (t-test). **d**, Mean $\Delta F/F$ values during the delay period for delay-preferring cells on trials with different behavioral parameters. Cells were separated by trial-type preference. Trials were separated by the mean values for each behavioral parameter during the delay period. $p > 0.05$ (t-test) for all comparisons.



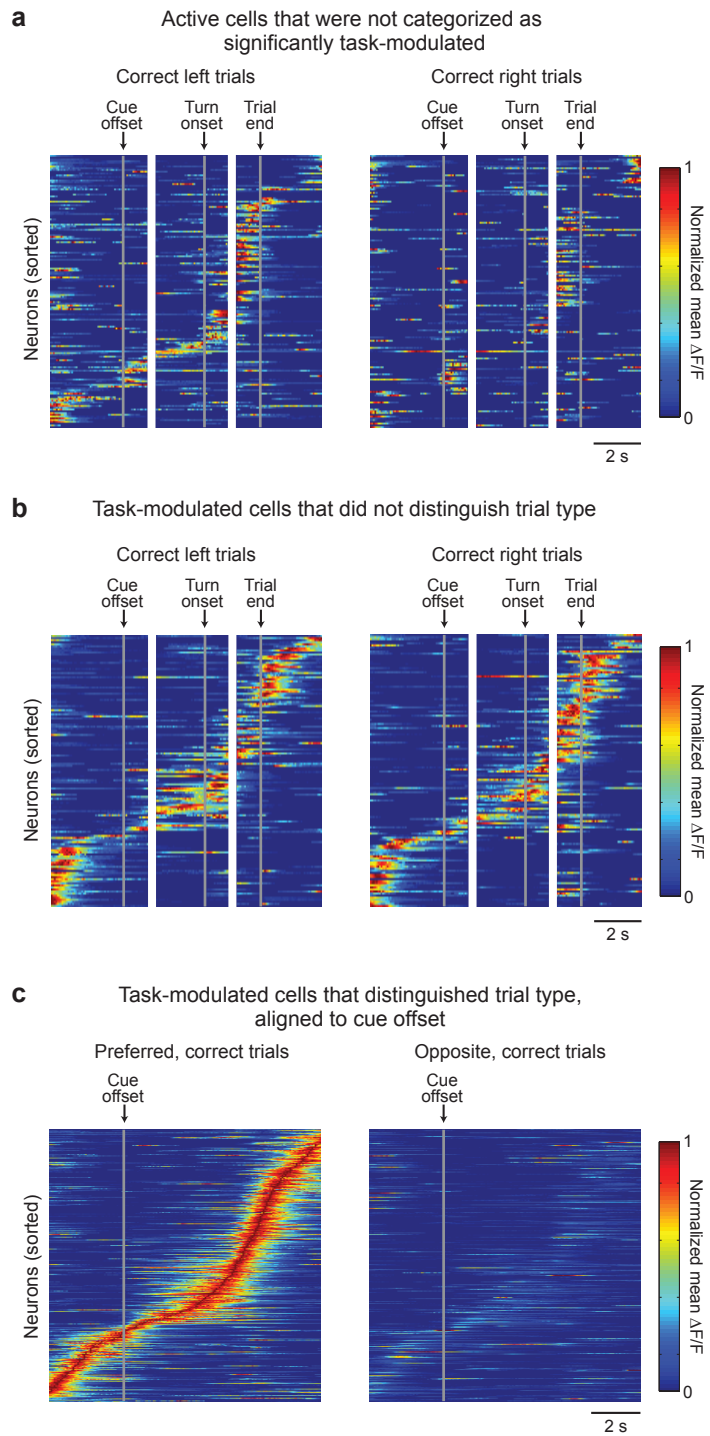
Supplementary Figure 4 | Identification of the PPC using retrograde and anterograde tracing. **a**, Retrogradely-transported beads were injected into the cortex. Labeled cell bodies at distant locations were identified following retrograde transport of the injected beads. A single coronal section is shown. **b**, List of areas that were labeled by the fluorescent beads, based on injections in 4 mice. **c**, Example images of labeling with the fluorescent beads. **d**, PPC neurons were labeled with GCaMP3 or GFP using viral methods. Labeled axons at distant sites were identified. **e**, Partial list of areas receiving axonal projections from the PPC. **f**, Example image of axonal labeling in the dorsal striatum and the mPFC. **g**, Example two-photon images of labeled axons in the lateral posterior thalamus in a histology section. The yellow arrows point out several examples of labeled axons. Note that retrogradely-labeled cell bodies are not present.



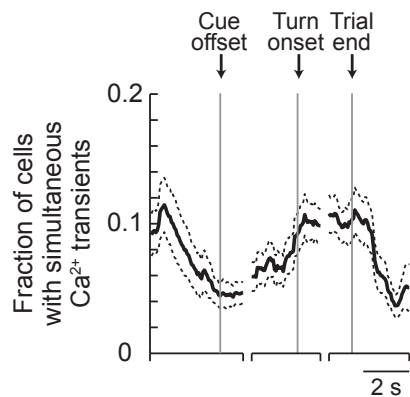
Supplementary Figure 5 | Categorization of cells by activity patterns. Details of the criteria for each category are described in the Methods.



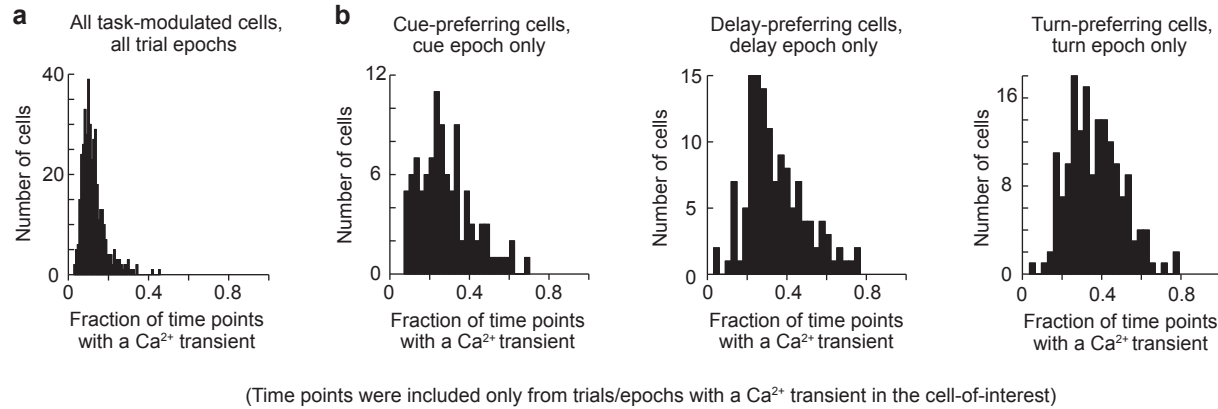
Supplementary Figure 6 | Example activity patterns of three PPC cells on individual trials. Top: Color-coded $\Delta F/F$ traces for individual correct left and right choice trials. Each row is a single trial aligned to the cue offset, turn onset, and trial end. Three cells are shown from left to right. Bottom: Mean $\Delta F/F$ traces for correct right (red) and left (blue) choice trials. Dashed lines indicate mean \pm sem.



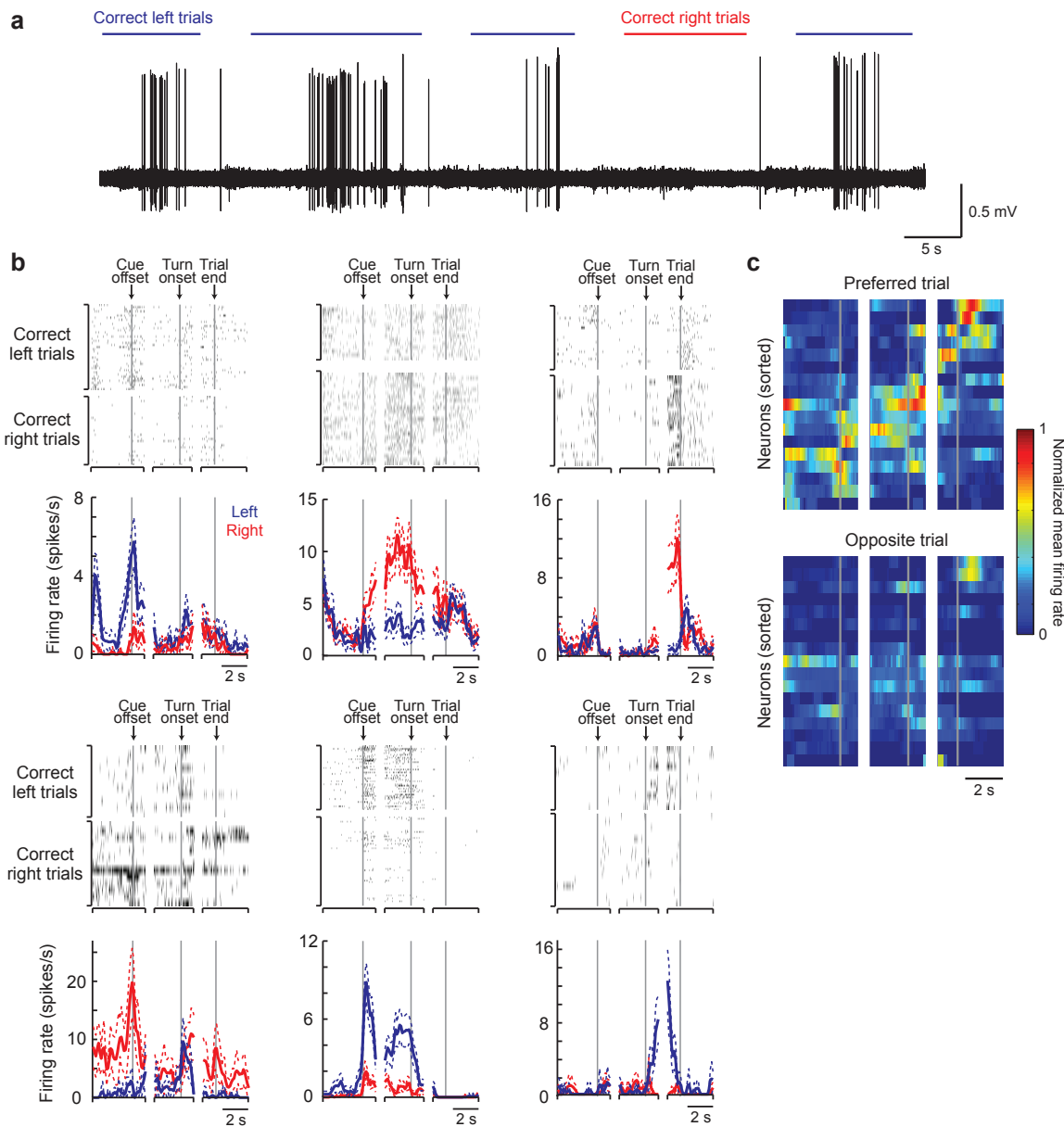
Supplementary Figure 7 | Activity patterns of PPC cells. **a**, Mean $\Delta F/F$ traces for active cells that were not task-modulated. Each row is an individual cell. The same cells are shown in matching rows for correct right and left choice trials. For each cell, $\Delta F/F$ values for left and right choice trials were normalized to the same value. **b**, Mean $\Delta F/F$ traces for the task-modulated cells that did not distinguish trial type. **c**, Mean $\Delta F/F$ traces for the choice-specific, task-modulated cells, as in Fig. 2d except that the traces are aligned only to the cue offset.



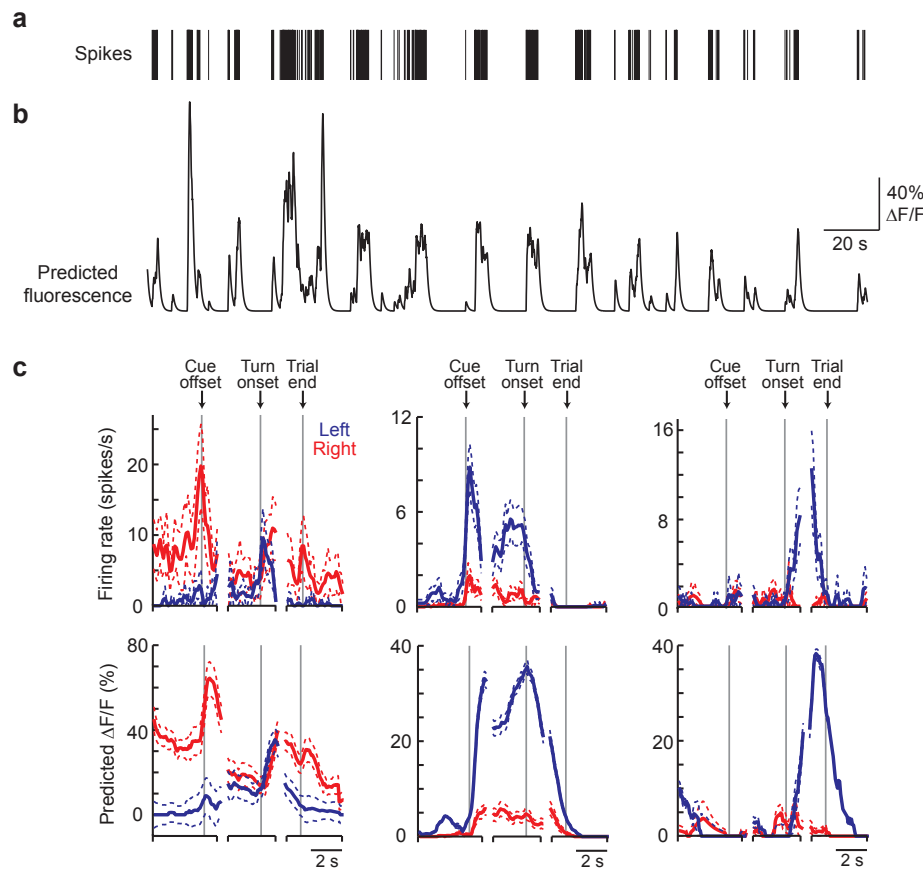
Supplementary Figure 8 | Fraction of cells (manually selected regions-of-interest) with simultaneous Ca²⁺ transients as a function of time during a trial. This is a measure of how many cells simultaneously have increased activity levels. The values are based on the ΔF/F time series, not the mean traces. The time of onset and offset of the transients in one cell relative to transients in other cells is ignored here.



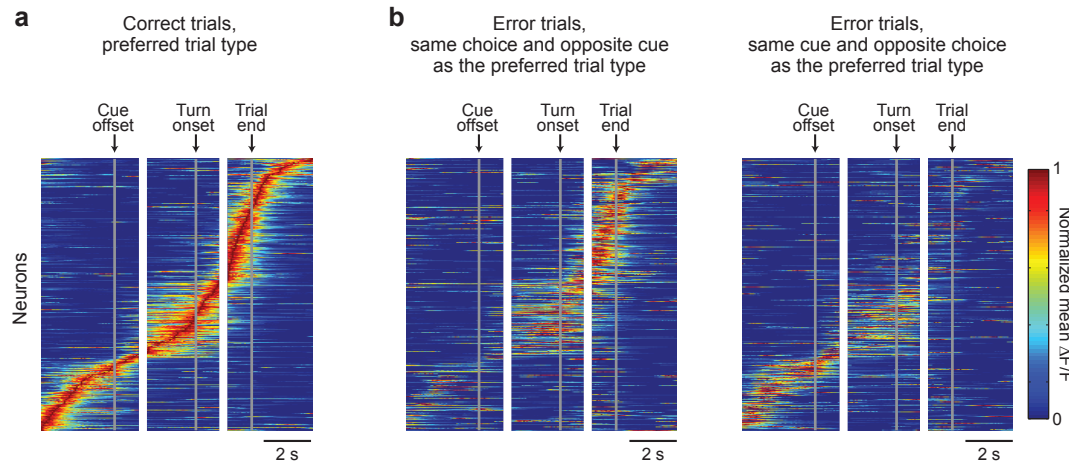
Supplementary Figure 9 | Activity durations of cells during trials. **a**, Histogram of the fraction of time points in a trial containing a Ca^{2+} transient for individual task-modulated cells. Time points were only considered in the trials in which there was a significant Ca^{2+} transient in the cell-of-interest. **b**, Histogram of the fraction of time points in an epoch containing a Ca^{2+} transient for individual cells preferring that epoch. Time points were only considered in the epochs in which there was a significant Ca^{2+} transient in the cell-of-interest. Data for cue-, delay-, and turn-preferring cells are shown from left to right.



Supplementary Figure 10 | Electrophysiology recordings of PPC cells. **a**, Example extracellular electrophysiology recording. Horizontal lines indicate the time points within correct left (blue) and right (red) choice trials. **b**, Example raster plots (top panels) and firing rates (bottom panels) for six example cells. In the raster plot, each row indicates a single trial and each black tick mark indicates a spike. In the firing rate, the dashed lines indicate mean \pm sem. **c**, Normalized mean firing rates during preferred and opposite trials. Each row is an individual cell.

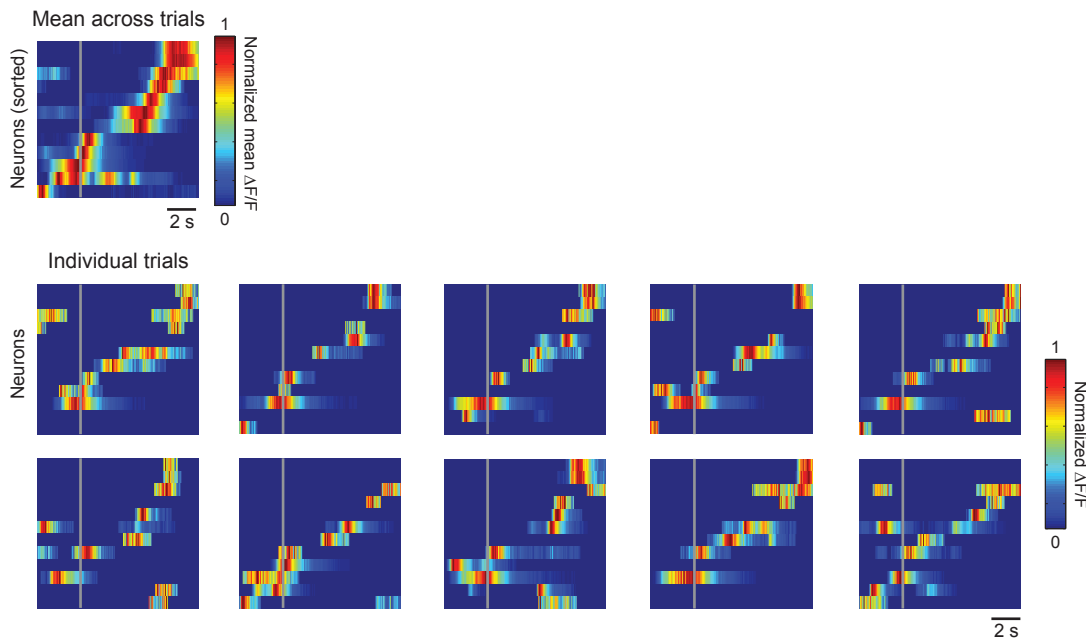


Supplementary Figure 11 | Mock $\Delta F/F$ traces based on electrophysiology recordings. **a**, Spike train from an extracellular electrophysiology recording. Each vertical line indicates a spike. **b**, Predicted fluorescence trace obtained by convolving the spike train from (a) with a calcium impulse response function (see Methods). **c**, Firing rates and predicted $\Delta F/F$ traces for three example cells. Dashed lines indicate mean \pm sem.

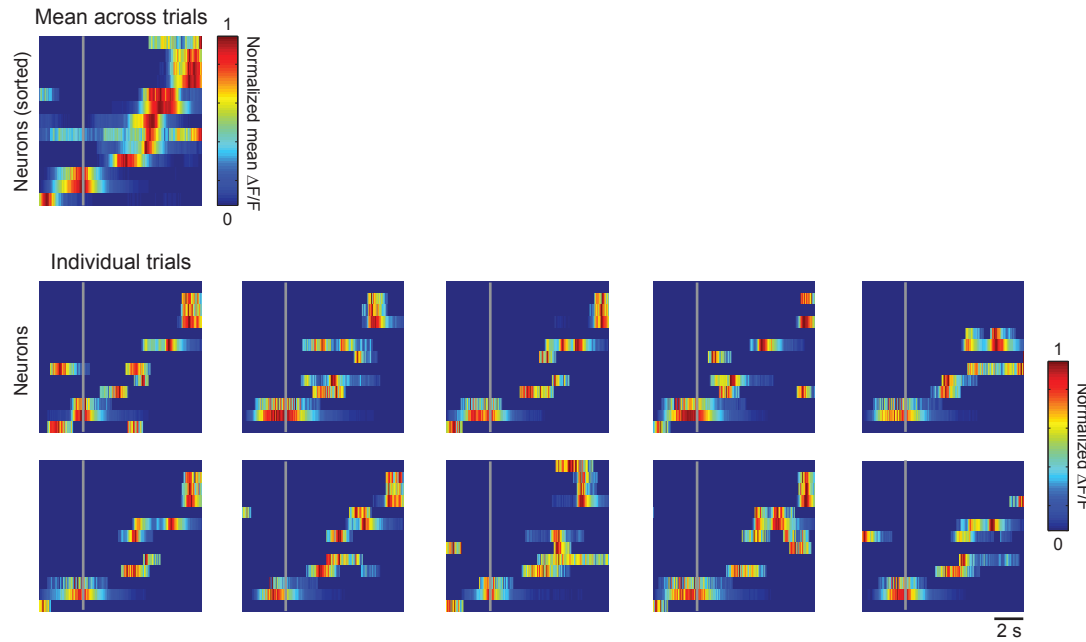


Supplementary Figure 12 | Neuronal activity on error trials. **a**, Normalized mean $\Delta F/F$ traces for individual choice-specific, task-modulated cells on each cell's preferred correct trials. This is the same plot as in Fig. 2d. **b**, Normalized mean $\Delta F/F$ traces for the same cells as in (a) except on error trials. Left: error trials in which the behavioral choice was the same as for the cell's preferred trial type and the cue was the opposite from the one in the preferred trial type. Right: error trials in which the cue was the same as for the preferred trial type and the behavioral choice was the opposite. The same rows in all plots correspond to the same cells. Mean $\Delta F/F$ traces for both error trial types were normalized to the same value.

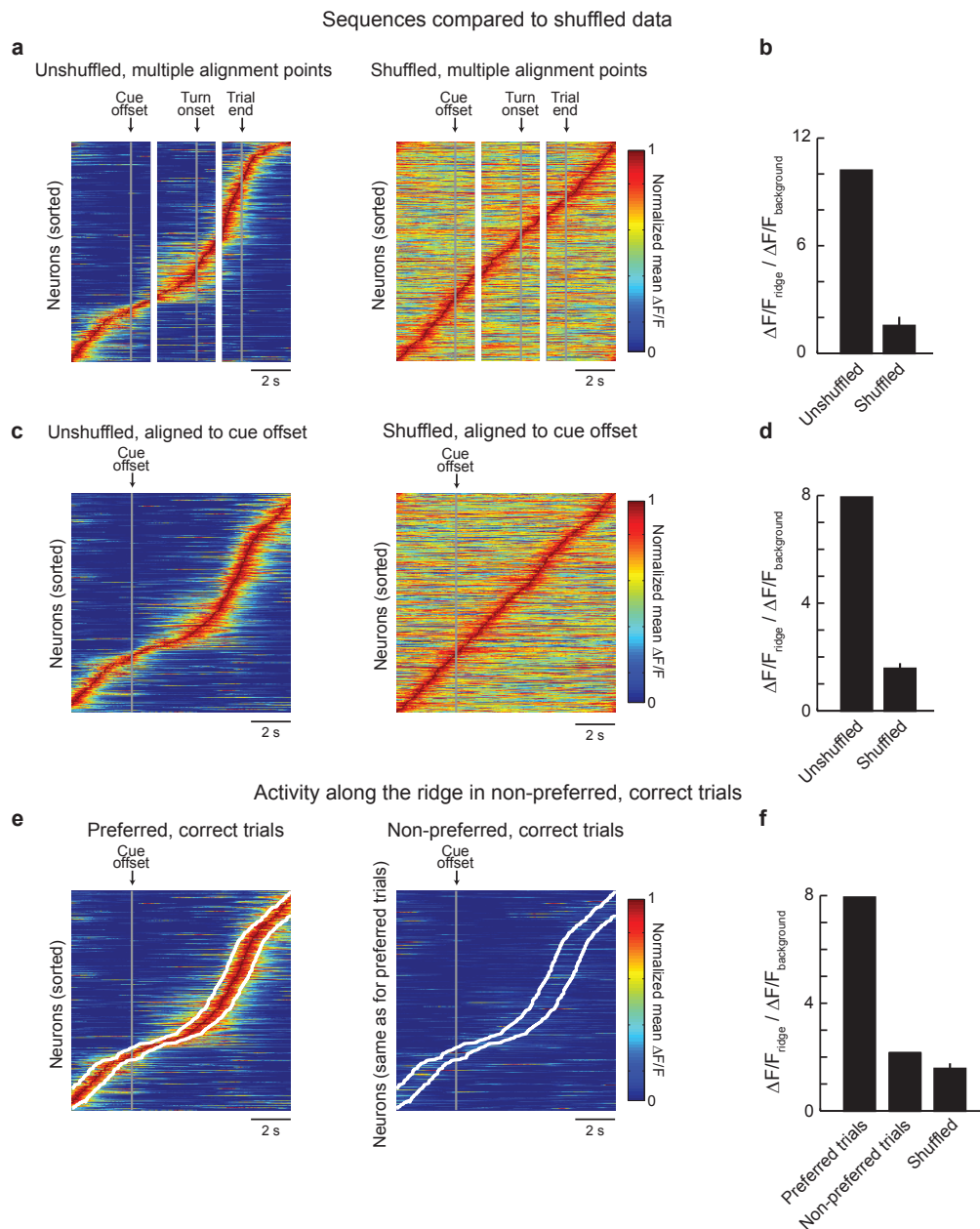
Example 1, simultaneously imaged choice-specific, task-modulated neurons on individual trials



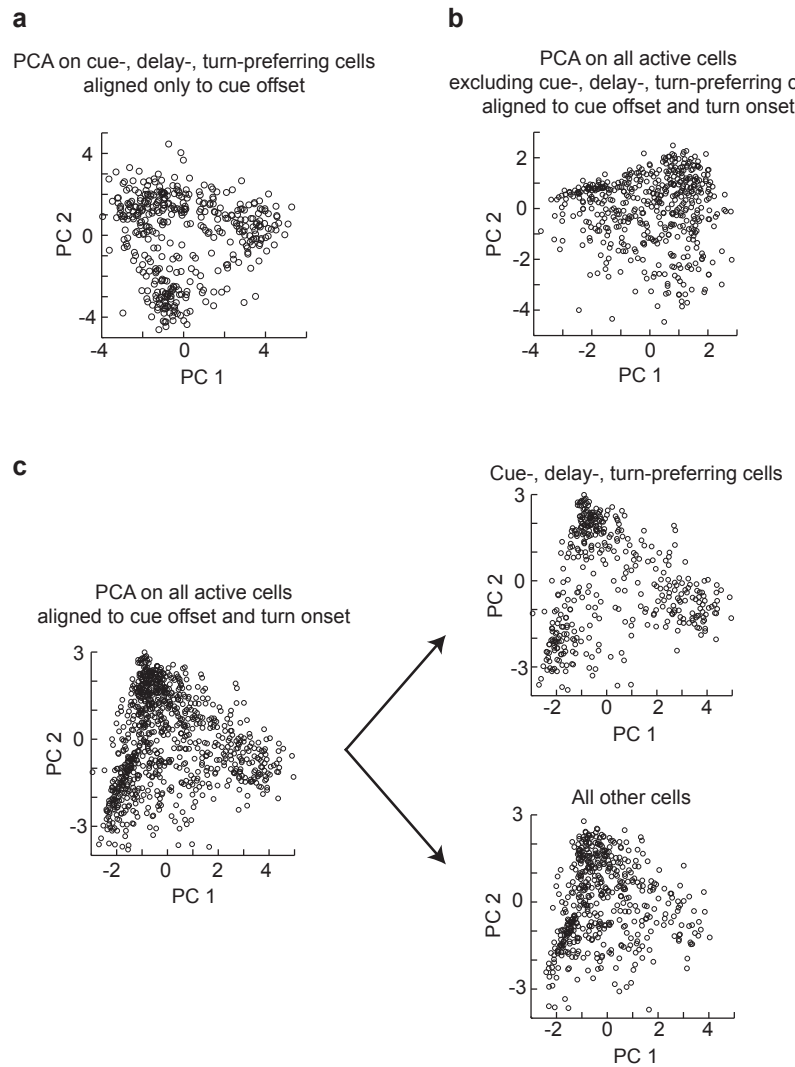
Example 2, simultaneously imaged choice-specific, task-modulated neurons on individual trials



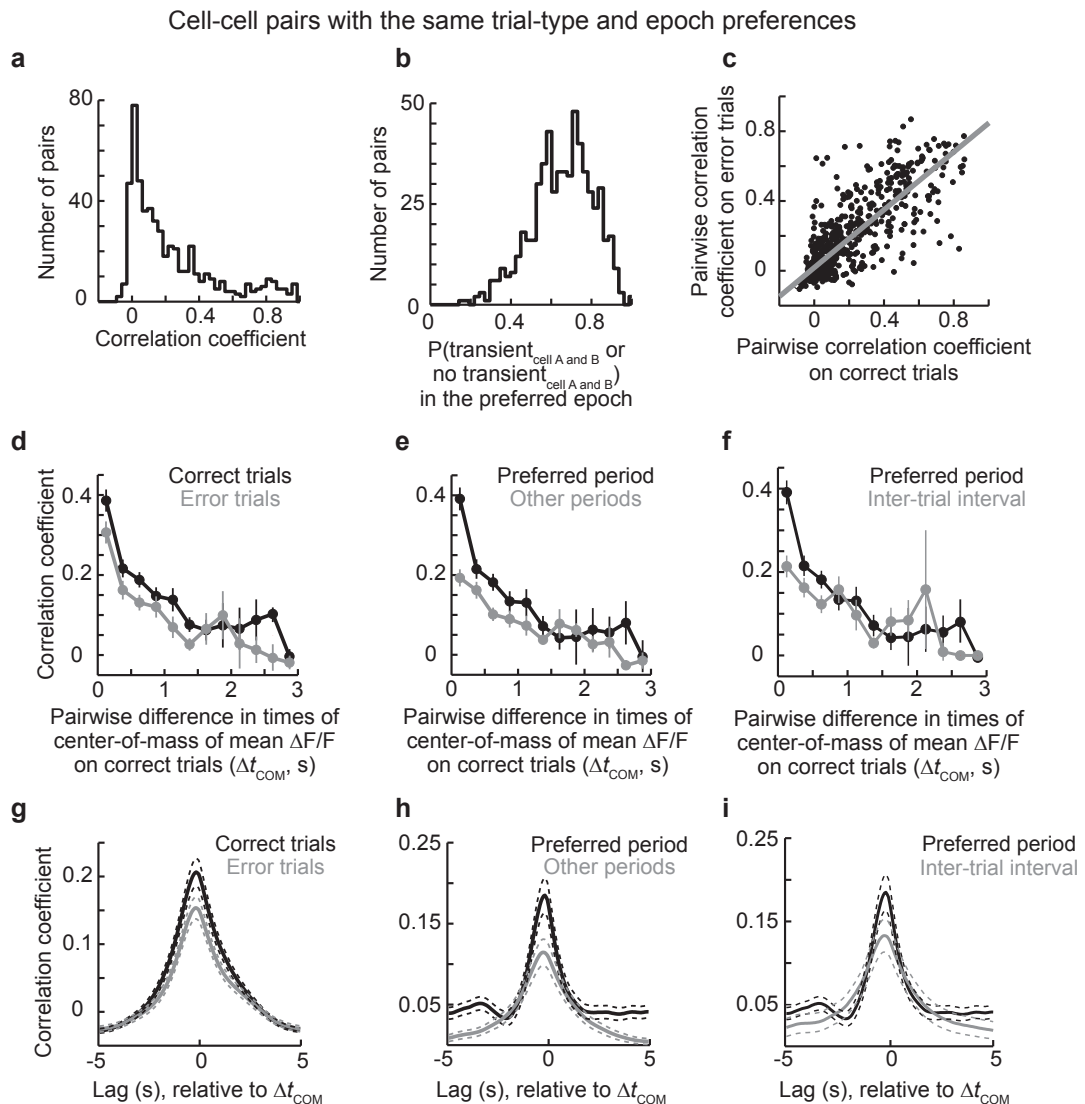
Supplementary Figure 13 | Sequences on individual trials. Examples from two imaging sessions are shown. The mean and individual trial $\Delta F/F$ values are plotted for right turn trial-preferring cells on correct right turn trials only. Neurons were sorted based on the mean $\Delta F/F$. Rows in the individual trials correspond to the same neurons as in the plot of the mean values. Data were aligned to the cue offset (gray line). Ten representative individual trials are shown. Note that sequences are apparent on individual trials, not only in the mean.



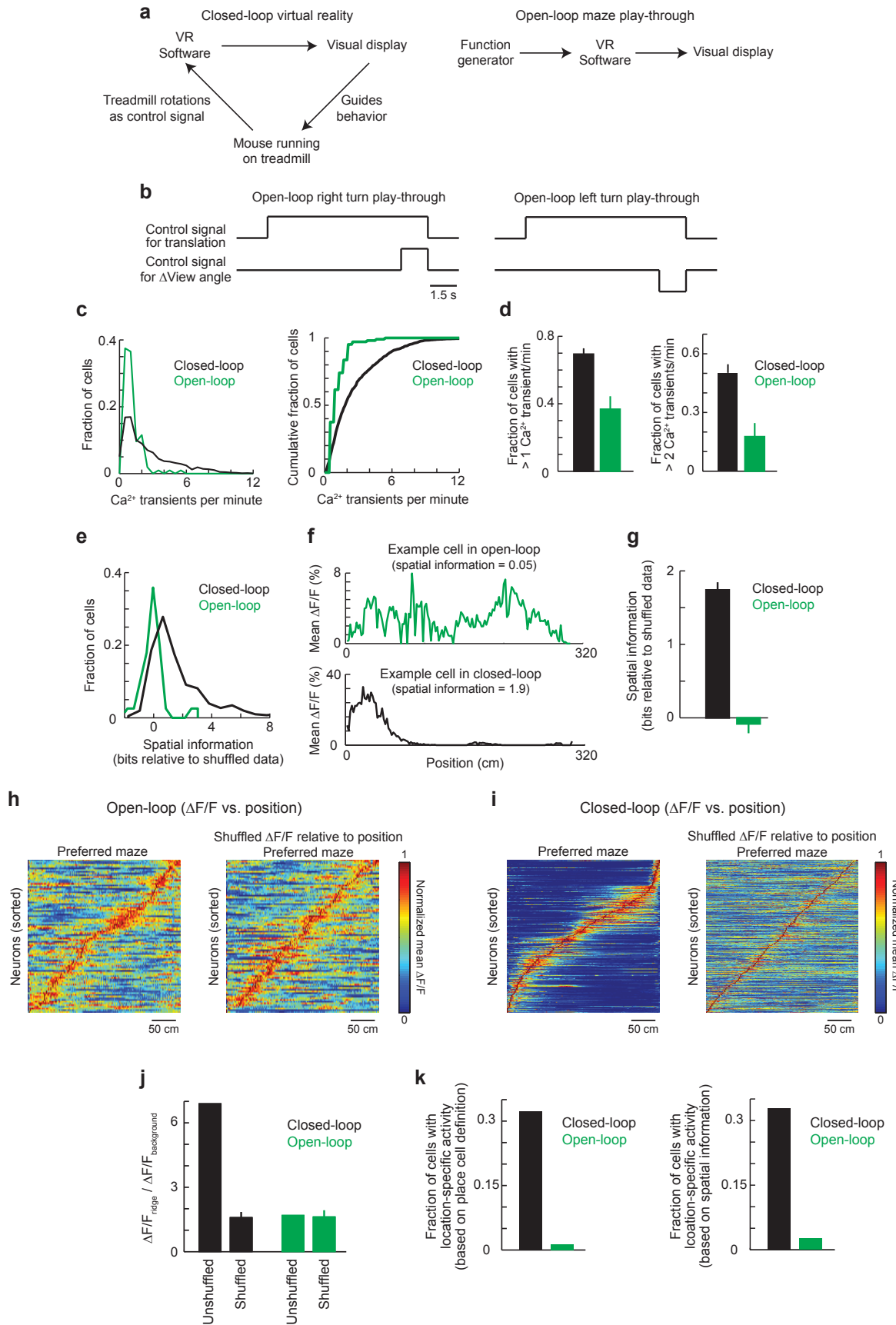
Supplementary Figure 14 | Comparison of sequences to shuffled datasets. **a**, Left: Activity of task-modulated, choice-specific neurons during their preferred trial type, as in Fig. 2d. Right: The same cells as in the left panel, except with shuffled $\Delta F/F$ traces. The non-averaged fluorescence time series for each cell was rotated by a random amount relative to the position values, and the mean $\Delta F/F$ values were re-calculated. The unshuffled and shuffled plots were sorted separately. Ordering data is expected to create a ridge along the diagonal. The relevant comparison is therefore between unshuffled data and shuffled data, which accounts for the effect of ordering the data. Note that different patterns are present in the shuffled and unshuffled data. **b**, Ridge-to-background $\Delta F/F$ ratio for the plots from (a). The ridge was defined as the 20 points surrounding the peak value, and the background was defined as all other points. The ridge-to-background ratio provides a measure of how selective the activity of the cell was during the task. A ridge-to-background ratio was calculated for each cell, and a mean value was calculated across all cells. Based on 1000 shuffles, $p < 0.001$ vs. shuffled. **c**, Same as in (a), except for $\Delta F/F$ traces aligned only to the cue offset. **d**, Same as in (b), except for $\Delta F/F$ traces aligned only to the cue offset. Based on 1000 shuffles, $p < 0.001$ vs. shuffled. **e**, Left: Same as in (c), except with the margins of the ridge outlined in white. Right: Same cells as in the left panel, except on the non-preferred, correct trials. Corresponding rows in the left and right panels are from the same cell. $\Delta F/F$ values were normalized by the peak mean $\Delta F/F$ in the preferred, correct trial. This plot illustrates that on non-preferred trials the same cells were not activated in the same sequence as on the preferred trials. **f**, Ridge-to-background ratio for the preferred trials, non-preferred trials, and shuffled data. $p < 0.001$ for preferred vs. non-preferred trials. Because the ridge-to-background on non-preferred trials was much lower than for the preferred trials and similar to the shuffled data, these results suggest that robust sequences of activation, using the same sequence of cells as on preferred trials, were not strongly present during non-preferred, correct trials.



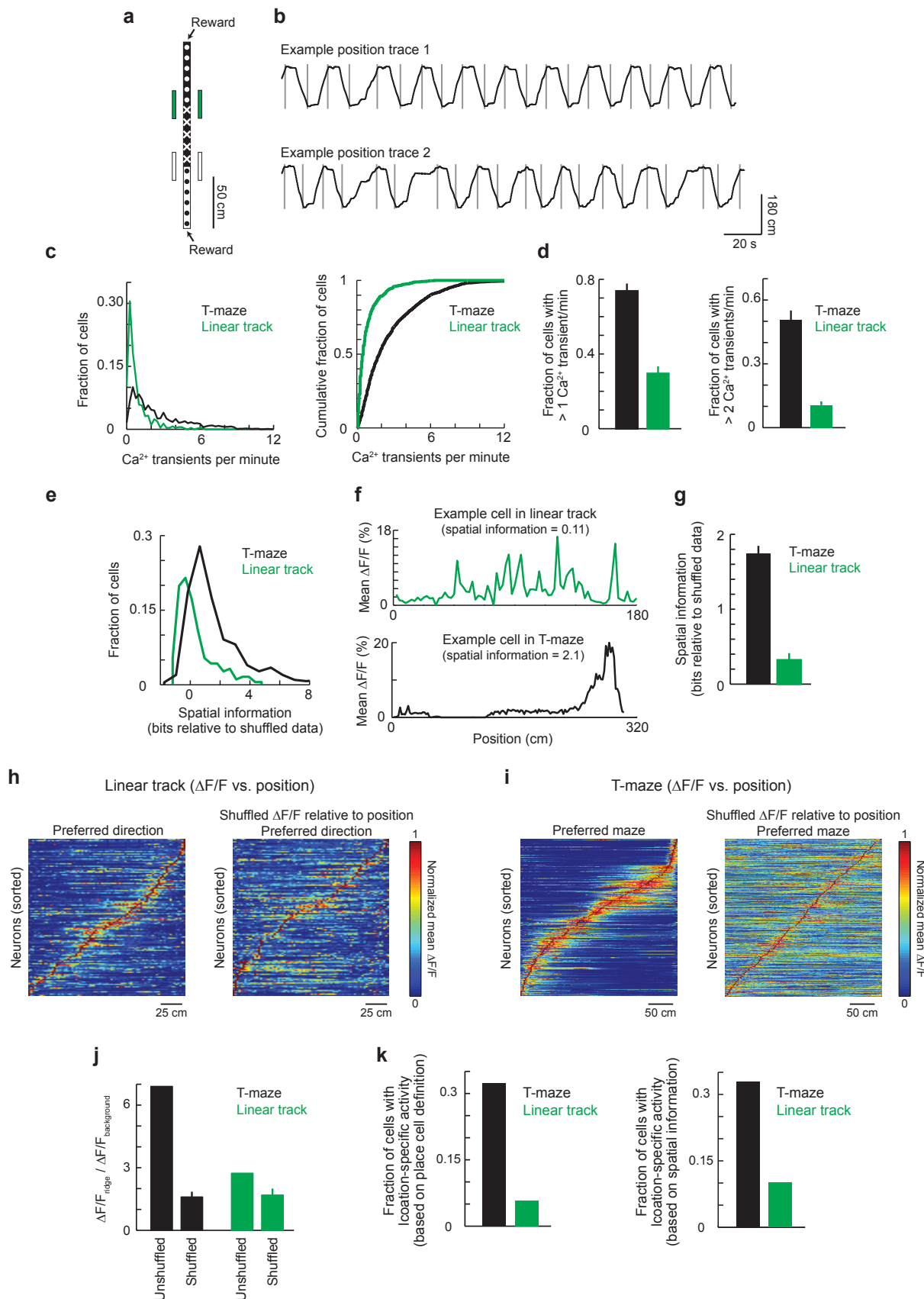
Supplementary Figure 15 | PCA to identify groups of cells. **a**, PCA on normalized mean $\Delta F/F$ traces, aligned only to the cue offset, for choice-specific, task-modulated cells. Alignment to the cue offset alone provided a continuous $\Delta F/F$ trace without gaps. Scores for the first two principal components are shown. Each point is an individual cell. **b**, PCA on normalized mean $\Delta F/F$ traces for all the active cells, excluding the choice-specific, task-modulated cells. **c**, PCA on normalized mean $\Delta F/F$ traces for all active cells. Following PCA, cells were divided and re-plotted separately for choice-specific, task-modulated cells and all other cells.



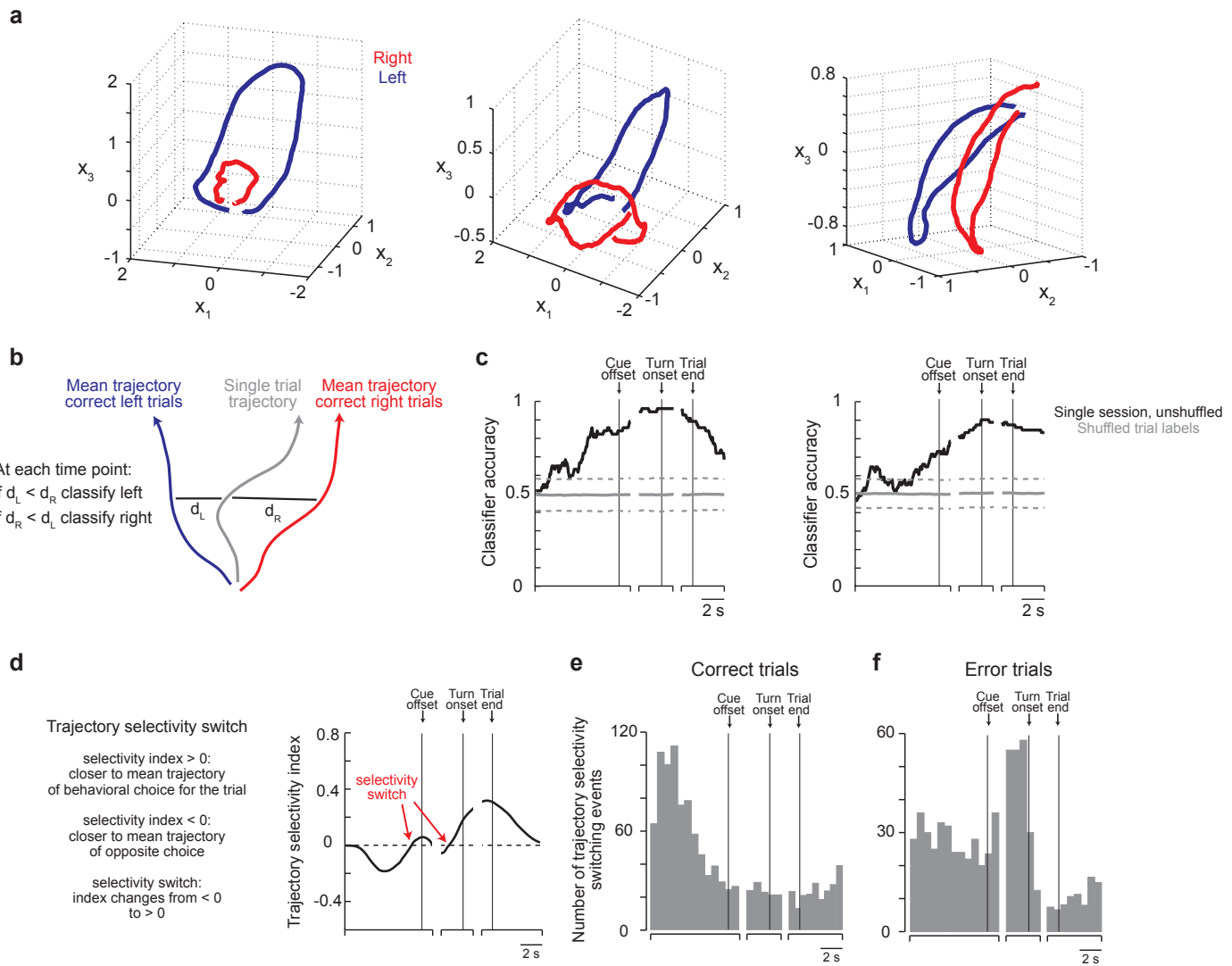
Supplementary Figure 16 | Correlations between cells during correct and error trials and during the inter-trial interval. **a**, Pearson's correlations on the non-averaged $\Delta F/F$ traces (all trial and inter-trial interval time points) for cell pairs with the same trial-type and behavioral period preferences ($n = 589$ pairs). The same pairs were used for (b-i). **b**, Probability that two cells either both had or both did not have a significant transient in their preferred behavioral period (all trials). Timing within the behavioral period was ignored. **c**, Correlations between $\Delta F/F$ traces for pairs of cells on correct and error trials. Correlations were calculated from the non-averaged $\Delta F/F$ traces. Each point is from a single pair of cells. The regression line is shown in gray. Spearman's correlation: $p = 0.77$, $p < 0.001$. **d**, Correlations between $\Delta F/F$ traces for pairs of cells on correct trials (black) and error trials (gray) as a function of the difference in the times of activity for a cell pair. The difference in the time of activity (Δt_{COM}) was defined based on t_{COM} calculated on correct trials only. **e**, Same as in (d) except for time points in the preferred period (black) and time points outside the preferred period (gray). **f**, Same as in (d) except for time points in the preferred period (black) and time points in the inter-trial interval (gray). **g**, Cross-correlation between the $\Delta F/F$ traces for the cell-cell pair on correct trials (black) and error trials (gray). Lags are relative to Δt_{COM} on correct trials only (i.e. lag = Δt_{COM} is plotted as 0 s on the x-axis). **h**, Same as in (g) except for time points in the preferred period (black) and time points outside the preferred period (gray). **i**, Same as in (g) except for time points in the preferred period (black) and time points in the inter-trial interval (gray).



Supplementary Figure 17 | Imaging PPC activity during open-loop movies of simulated runs through the T-maze. **a**, Description of closed-loop virtual reality versus open-loop play-through experiments. In the closed-loop experiments, rotations of the treadmill triggered by the mouse control movement through the environment. In the open-loop experiments, the treadmill does not control the environment; rather, the environment is played to the mouse. **b**, Control signals used to generate a play-through of the T-maze. These signals were input into the channels that typically receive the signals from the optical computer mouse recording treadmill rotational velocities. **c**, Histogram (left) and cumulative distribution (right) of Ca^{2+} transient rates for the closed-loop (black) and open-loop (green) experiments. Data are from all imaged areas from all mice (closed-loop: $n = 6$ mice; open-loop: $n = 3$ mice). Different mice were used for the different experiments. **d**, Fraction of cells with more than 1 (left) or 2 (right) Ca^{2+} transients per minute. Each bar represents the mean \pm sem. Each data point was the fraction of cells meeting the transient rate criterion in a single imaged area (closed-loop: $n = 29$; open-loop: $n = 24$ areas). **e**, Histogram of spatial information content in PPC neuronal activity patterns during the closed-loop (black) and open-loop (green) experiments. Spatial information content was computed by comparison to shuffled datasets. See Methods for details. **f**, Example plots of mean $\Delta F/F$ versus linearized position in the T-maze. The spatial information values correspond to examples from cells in (e). **g**, Mean spatial information content. The bars indicate mean \pm sem, with one data point per cell. **h**, Left: Activity patterns during the open-loop experiments. Each row is the normalized mean $\Delta F/F$ for an individual cell as a function of position in the T-maze. The T-maze position was linearized from the start of the trial through the turn at the intersection in 2.25 cm bins. A cell's preferred maze was the one in which it had a higher mean $\Delta F/F$; values were only considered for a cell's preferred maze. The cells were sorted by the peak of the mean $\Delta F/F$. All cells with a Ca^{2+} transient rate of higher than 0.5 transients/min were included. Right: The same cells as in the left panels, except now with shuffled $\Delta F/F$ traces. The non-averaged $\Delta F/F$ time series for each cell were rotated by a random amount relative to the position values, and the mean $\Delta F/F$ values were re-calculated. The rows between the unshuffled and shuffled plots do not correspond to the same cells because each was sorted separately. We note that ordering data by the peak activity time is expected to create a ridge along the diagonal. The relevant comparison is therefore between unshuffled data and shuffled data, which accounts for the effect of ordering the data. Note that similar patterns are present in the shuffled and unshuffled data. **i**, Same as in (h), except for the closed-loop T-maze data. All cells with a Ca^{2+} transient rate of higher than 0.5 transients/min were included, even if they were not choice-specific or task-modulated. Note the difference between the unshuffled and shuffled data. **j**, Ridge-to-background $\Delta F/F$ ratio for the plots from (h-i). The ridge was defined as the 20 spatial bins surrounding the peak value, and the background was defined as all other spatial bins. The ridge-to-background ratio provides a measure of how selective the activity of the cell was during the task. A ridge-to-background ratio was calculated for each cell. The mean value across all cells was used to compare with shuffled versions of the data. Based on 1000 shuffles, $p < 0.001$ for closed-loop vs. shuffled and $p > 0.4$ for open-loop vs. shuffled. $p < 0.001$ for closed-loop vs. open-loop. **k**, Fraction of cells in the open-loop (green) and closed-loop (black) experiments with place-specific activity. Place-specific activity was determined using criteria previously used for defining hippocampal place cells (left; see Methods), or using the spatial information content (right). These measures provide a quantification of whether the cells were modulated by specific aspects of the task or the play-through.



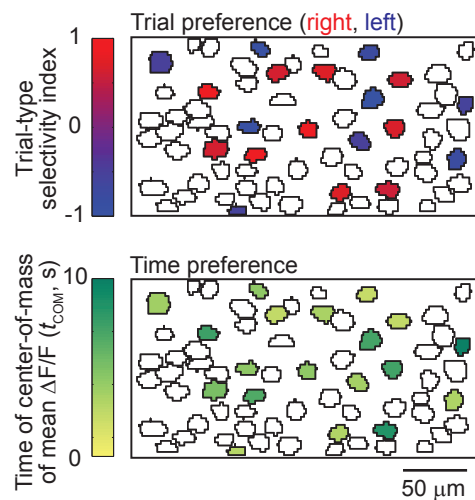
Supplementary Figure 18 | Imaging PPC activity during a linear track task. **a**, Schematic of the linear track. The linear track contained wall patterns identical to those used in the T-maze. The width of the linear track was identical to the width of the T-maze. **b**, Example position traces during the linear track task. The mouse had to run to one end of the track to receive a reward (gray lines) and then run to the opposite end to receive the next reward. Note that the task required running straight down the track followed by turning around at the end of the track. **c**, Histogram (left) and cumulative distribution (right) of Ca^{2+} transient rates for the T-maze (black) and linear track (green) experiments. Data are from all imaged areas from all mice (T-maze: $n = 6$ mice; linear track: $n = 3$ mice). Different mice were used for the different experiments. **d**, Fraction of cells with more than 1 (left) or 2 (right) Ca^{2+} transients per minute. Each bar represents the mean \pm sem. Each data point was the fraction of cells meeting the transient rate criterion in a single imaged area (T-maze: $n = 29$; linear track: $n = 9$ areas). **e**, Histogram of spatial information content in PPC neuronal activity patterns during the T-maze (black) and linear track (green) experiments. Spatial information content was computed by comparison to shuffled datasets. See Methods for details. **f**, Example plots of mean $\Delta F/F$ versus position in the T-maze or linear track. The spatial information values correspond to examples from cells in (e). **g**, Mean spatial information content. The bars indicate mean \pm sem, with one data point per cell. **h**, Left: Activity patterns during the linear track experiments. Each row is the normalized mean $\Delta F/F$ for an individual cell as a function of position (2.25 cm bins). A cell's preferred direction was the one in which it had a higher mean $\Delta F/F$; values were only considered for a cell's preferred direction of running. The cells were sorted by the peak of the mean $\Delta F/F$. All cells with a Ca^{2+} transient rate of higher than 0.5 transients/min were included. Right: The same cells as in the left panels, except now with shuffled $\Delta F/F$ traces. The non-averaged $\Delta F/F$ time series for each cell were rotated by a random amount relative to the position values, and the mean $\Delta F/F$ values were re-calculated. The rows between the unshuffled and shuffled plots do not correspond to the same cells because each was sorted separately. We note that ordering data by the peak activity time is expected to create a ridge along the diagonal. The relevant comparison is therefore between unshuffled data and shuffled data, which accounts for the effect of ordering the data. Note that similar patterns are present in the shuffled and unshuffled data. **i**, Same as in (h), except for the T-maze data. All cells with a Ca^{2+} transient rate of higher than 0.5 transients/min were included, even if they were not choice-specific or task-modulated. Note the difference between the unshuffled and shuffled data. **j**, Ridge-to-background $\Delta F/F$ ratio for the plots from (h-i). The ridge was defined as the 20 spatial bins surrounding the peak value, and the background was defined as all other spatial bins. The ridge-to-background ratio provides a measure of how selective the activity of the cell was during the task. A ridge-to-background ratio was calculated for each cell. The mean value across all cells was used to compare with shuffled versions of the data. Based on 1000 shuffles, $p < 0.001$ for the T-maze vs. shuffled and $p < 0.05$ for the linear track vs. shuffled. $p < 0.001$ for the T-maze vs. the linear track. **k**, Fraction of cells in the linear track (green) and T-maze (black) experiments with place-specific activity. Place-specific activity was determined using criteria previously used for defining hippocampal place cells (left; see Methods), or using the spatial information content (right). These measures provide a quantification of whether the cells were modulated by specific aspects of the task or the play-through.



Supplementary Figure 19 | Neuronal circuit trajectories. **a**, Example neuronal circuit trajectories from three sessions from different fields-of-view. The mean trajectories for correct right (red) and left (blue) choice trials are shown. **b**, Schematic of a classification scheme based on distances to the mean trajectories. At each time point the distance from the trajectory on a single trial to the mean right and left choice trajectories was measured (d_R , d_L). If d_R was less than d_L , the trial at that time point was classified as ‘right choice’, and vice versa. **c**, Statistics for classification accuracy. Data from two example sessions are shown. The black line indicates the classification accuracy on the unshuffled data. The gray line indicates the classification accuracy with shuffled trial labels. Dashed lines indicate the 95% confidence interval. 1000 shuffles were performed. **d**, Switches between trajectories on individual trials. For individual trial trajectories, a trajectory selectivity index was defined as

$$(d_{\text{to mean traj, opposite choice}} - d_{\text{to mean traj, same choice}}) / (d_{\text{to mean traj, same choice}} + d_{\text{to mean traj, opposite choice}})$$

where the mean trajectories were defined using correct trials only. Selectivity switches were defined as time points when the trajectory changed from closer to the trajectory of the choice opposite the behavioral choice for that trial (index < 0) to closer to the trajectory of the same choice as the behavioral choice for that trial (index > 0). Multiple switch events were possible on single trials. Right: schematic of selectivity switches. **e**, Histogram of times at which selectivity switches occurred on correct trials. **f**, Histogram of times at which selectivity switches occurred on error trials.



Supplementary Figure 20 | Relative anatomical location of PPC activity patterns. Example field-of-view with all cells outlined and choice-specific, task-modulated cells colored. Top: Cells' trial-type selectivity, defined as $(\Delta F/F_{\text{right trials}} - \Delta F/F_{\text{left trials}}) / (\Delta F/F_{\text{right trials}} + \Delta F/F_{\text{left trials}})$. Values close to 1 (red) and -1 (blue) indicate right and left choice preferences, respectively. Bottom: Cells' time of the center-of-mass of the mean $\Delta F/F$ trace (t_{COM}). $t_{\text{COM}} = 0$ corresponds to ~ 3 s before the cue offset.

Linear regression analysis for delay-preferring cells during the delay period

Choice only: $F = \beta_0 + \beta_1 C + \varepsilon$ (Eq. 1)

Choice and other behavioral parameters: $F = \beta_0 + \beta_1 C + \beta_2 P + \beta_3 V + \beta_4 R_1 + \beta_5 R_2 + \varepsilon$ (Eq. 2)

F : $\Delta F/F$ values

C : choice (0 for right turn, 1 for left turn)

P : lateral position (short dimension of maze)

V : view angle

R_1 : treadmill rotational velocity for translation

R_2 : treadmill rotational velocity for view angle changes

β_0 : constant coefficient

β_{1-5} : fitted coefficients

ε : error term

	Fraction of delay-preferring cells with a significant effect of choice during the delay period	Fraction of delay-preferring cells with a significant effect of other parameters during the delay period
Choice predictor only (Eq. 1)	99%	NA
Choice + other predictors (Eq. 2)	78%	18%

Supplementary Table 1 | Regression analysis of parameters potentially influencing the activity of delay-preferring cells during the delay period. First, trial type or behavioral choice (right or left trial) was used as the only predictor (Equation 1). Next, additional behavioral parameters were included (Equation 2). Based on the results from the regression using Equation 2, the behavioral parameters other than trial type cannot account for the activity patterns we observed.